# Pseudo-Riemannian Graph Convolutional Networks

**Bo Xiong**[*]
University of Stuttgart
Stuttgart, Germany

**Shichao Zhu**[*]
IIE, Chinese Academy of Sciences
Beijing, China

**Nico Potyka**
Imperial College London
London, United Kingdom

**Shirui Pan**
Griffith University
Queensland, Australia

**Chuan Zhou**
AMSS, Chinese Academy of Sciences
Beijing, China

**Steffen Staab**
University of Stuttgart
University of Southampton
Stuttgart, Germany

## Abstract

Graph convolutional networks (GCNs) are powerful frameworks for learning embeddings of graph-structured data. GCNs are traditionally studied through the lens of Euclidean geometry. Recent works find that non-Euclidean Riemannian manifolds provide specific inductive biases for embedding hierarchical or spherical data. However, they cannot align well with data of mixed graph topologies. We consider a larger class of pseudo-Riemannian manifolds that generalize hyperboloid and sphere. We develop new geodesic tools that allow for extending neural network operations into geodesically disconnected pseudo-Riemannian manifolds. As a consequence, we derive a pseudo-Riemannian GCN that models data in pseudo-Riemannian manifolds of constant nonzero curvature in the context of graph neural networks. Our method provides a geometric inductive bias that is sufficiently flexible to model mixed heterogeneous topologies like hierarchical graphs with cycles. We demonstrate the representational capabilities of this method by applying it to the tasks of graph reconstruction, node classification and link prediction on a series of standard graphs with mixed topologies. Empirical results demonstrate that our method outperforms Riemannian counterparts when embedding graphs of complex topologies.

## 1 Introduction

Learning from graph-structured data is a pivotal task in machine learning, for which graph convolutional networks (GCNs) [1, 2, 3, 4] have emerged as powerful graph representation learning techniques. GCNs exploit both features and structural properties in graphs, which makes them well-suited for a wide range of applications. For this purpose, graphs are usually embedded in Riemannian manifolds equipped with a positive definite metric. Euclidean geometry is a special case of Riemannian manifolds of constant zero curvature that can be understood intuitively and has well-defined operations. However, the representation power of Euclidean space is limited [5], especially when embedding complex graphs exhibiting hierarchical structures [6]. Non-Euclidean Riemannian manifolds of constant curvatures provide an alternative to accommodate specific graph topologies. For example, hyperbolic manifold of constant negative curvature has exponentially growing volume and is well suited to represent hierarchical structures such as tree-like graphs [7, 8, 9, 10]. Similarly, spherical manifold of constant positive curvature is suitable for embedding spherical data in various fields [11, 12, 13] including graphs with cycles. Some recent works [14, 15, 16, 17, 18] have extended GCNs to such non-Euclidean manifolds and have shown substantial improvements.

---

[*]Equal contribution. Correspondence to bo.xiong@ipvs.uni-stuttgart.de

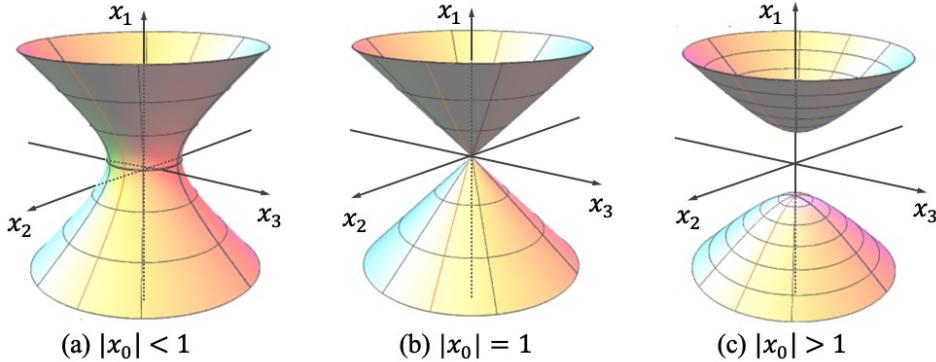(a) $|x_0| < 1$        (b) $|x_0| = 1$        (c) $|x_0| > 1$

Figure 1: The different submanifolds of a four-dimensional pseudo-hyperboloid of curvature $-1$ with two time dimensions. By fixing one time dimension $x_0$, the induced submanifolds include (a) an one-sheet hyperboloid, (b) the double cone, and (c) a two-sheet hyperboloid.

The topologies in real-world graphs [6], however, usually exhibit highly heterogeneous topological structures, which are best represented by different geometrical curvatures. A globally homogeneous geometry lacks the flexibility for modeling complex graphs [19]. Instead of using a single manifold, product manifolds [19, 20] combining multiple Riemannian manifolds have shown advantages when embedding graphs of mixed topologies. However, the curvature distribution of product manifolds is the same at each point, which limits the capability of embedding topologically heterogeneous graphs. Furthermore, Riemannian manifolds are equipped with a positive definite metric disallowing for the faithful representation of the negative eigen-spectrum of input similarities [21].

Going beyond Riemannian manifolds, pseudo-Riemannian manifolds equipped with indefinite metrics constitute a larger class of geometries, pseudo-Riemannian manifolds of constant nonzero curvature do not only generalize the hyperbolic and spherical manifolds, but also contain their submanifolds (Cf. Fig. 1), thus providing inductive biases specific to these geometries. Pseudo-Riemannian geometry with constant zero curvature (i.e. Lorentzian spacetime) was applied to manifold learning for preserving local information of non-metric data [5] and embedding directed acyclic graph [22]. To model complex graphs containing both hierarchies and cycles, pseudo-Riemannian manifolds with constant nonzero curvature have recently been applied into graph embeddings using non-parametric learning [23, 24, 25], but the representation power of these works is not on par with the Riemannian counterparts yet, mostly because of the absence of geodesic tools to extend neural network operations into pseudo-Riemannian geometry.

In this paper, we take the first step to extend GCNs into pseudo-Riemannian manifolds foregoing the requirement to have a positive definite metric. Exploiting pseudo-Riemannian geometry for GCNs is non-trivial because of the *geodesical disconnectedness* in pseudo-Riemannian geometry. There exist broken points that cannot be smoothly connected by a geodesic, leaving necessary geodesic tools undefined. To deal with it, we develop novel geodesic tools that empower manipulating representations in geodesically disconnected pseudo-Riemannian manifolds. We make it by finding diffeomorphic manifolds that provide alternative geodesic operations that smoothly avoid broken cases. Subsequently, we generalize GCNs to learn representations of complex graphs in pseudo-Riemannian geometry by defining corresponding operations such as *linear transformation* and *tangential aggregation*. Different from previous works, the initial features of GCN could be fully defined in the Euclidean space. Thanks to the diffeomorphic operation that is bijective and differentiable, the standard gradient descent algorithm can be exploited to perform optimization.

To summarize, our main contributions are as follows: 1) We present neural network operations in pseudo-Riemannian manifolds with novel geodesic tools, to stimulate the applications of pseudo-Riemannian geometry in geometric deep learning. 2) We present a principled framework, pseudo-Riemannian GCN, which generalizes GCNs into pseudo-Riemannian manifolds with indefinite metrics, providing more flexible inductive biases to accommodate complex graphs with mixed topologies. 3) Extensive evaluations on three standard tasks demonstrate that our model outperforms baselines that operate in Riemannian manifolds. Source code is open available at https://github.com/xiongbo010/QGCN.

## 2 Preliminaries

### 2.1 Pseudo-Riemannian manifolds

A pseudo-Riemannian manifold [26] $(\mathcal{M}, g)$ is a smooth manifold $\mathcal{M}$ equipped with a nondegenerate and indefinite metric tensor $g$. Nondegeneracy means that for a given $\boldsymbol{\xi} \in \mathcal{T}_\mathbf{x}\mathcal{M}$, for any $\boldsymbol{\zeta} \in \mathcal{T}_\mathbf{x}\mathcal{M}$ we have $g_\mathbf{x}(\boldsymbol{\xi}, \boldsymbol{\zeta}) = 0$, then $\boldsymbol{\xi} = \mathbf{0}$. The metric tensor $g$ induces a scalar product on the *tangent* space $\mathcal{T}_\mathbf{x}\mathcal{M}$ for each point $\mathbf{x} \in \mathcal{M}$ such that $g_\mathbf{x} : \mathcal{T}_\mathbf{x}\mathcal{M} \times \mathcal{T}_\mathbf{x}\mathcal{M} \to \mathbb{R}$, where the *tangent* space $\mathcal{T}_\mathbf{x}\mathcal{M}$ can be seen as the first order local approximation of $\mathcal{M}$ around point $\mathbf{x}$. The elements of $\mathcal{T}_\mathbf{x}\mathcal{M}$ are called tangent vectors. *Indefinity* means that the metric tensor could be of arbitrary signs. A principal special case is the Riemannian geometry, where the metric tensor is positive definite (i.e. $\forall \boldsymbol{\xi} \in \mathcal{T}_\mathbf{x}\mathcal{M}, g_\mathbf{x}(\boldsymbol{\xi}, \boldsymbol{\xi}) > 0$ iff $\boldsymbol{\xi} \neq \mathbf{0}$).

**Pseudo-hyperboloid** By analogy with hyperboloid and sphere in Euclidean space. Pseudo-hyperboloids are defined as the submanifolds in the ambient pseudo-Euclidean space $\mathbb{R}^{s,t+1}$ with the dimensionality of $d = s + t + 1$ that uses the scalar product as $\forall \mathbf{x}, \mathbf{y} \in \mathbb{R}^{s,t+1}, \langle \mathbf{x}, \mathbf{y} \rangle_t = -\sum_{i=0}^{t} x_i y_i + \sum_{j=t+1}^{s+t} x_j y_j$. The scalar product induces a norm $\|\mathbf{x}\|_t^2 = \langle \mathbf{x}, \mathbf{x} \rangle_t$ that can be used to define a pseudo-hyperboloid $\mathcal{Q}_\beta^{s,t} = \left\{ \mathbf{x} = (x_0, x_1, \cdots, x_{s+t})^\top \in \mathbb{R}^{s,t+1} : \|\mathbf{x}\|_t^2 = \beta \right\}$, where $\beta$ is a nonzero real number parameter of curvature. $\mathcal{Q}_\beta^{s,t}$ is called *pseudo-sphere* when $\beta > 0$ and *pseudo-hyperboloid* when $\beta < 0$. Since $\mathcal{Q}_\beta^{s,t}$ is interchangeable with $\mathcal{Q}_{-\beta}^{t+1,s-1}$, we consider the pseudo-hyperbololid here. Following the terminology of special relativity, a point in $\mathcal{Q}_\beta^{s,t}$ can be interpreted as an event [5], where the first $t + 1$ dimensions are time dimensions and the last $s$ dimensions are space dimensions. Hyperbolic $\mathbb{H}$ and spherical $\mathbb{S}$ manifolds can be defined as the special cases of pseudo-hyperboloids by setting all time dimensions except one to be zero and setting all space dimensions to be zero, respectively, i.e. $\mathbb{H}_\beta = \mathcal{Q}_\beta^{s,1}, \mathbb{S}_{-\beta} = \mathcal{Q}_\beta^{0,t}$.

### 2.2 Geodesic tools of pseudo-hyperboloid

**Geodesic** A generalization of a *straight-line* in the Euclidean space to a manifold is called the *geodesic* [14, 27]. Formally, a geodesic $\gamma$ is defined as a constant speed curve $\gamma : \tau \mapsto \gamma(\tau) \in \mathcal{M}, \tau \in [0, 1]$ joining two points $\mathbf{x}, \mathbf{y} \in \mathcal{M}$ that minimizes the length, where the length of a curve is given by $L(\gamma) = \int_0^1 \sqrt{\left\| \frac{d}{dt} \gamma(\tau) \right\|_{\gamma(\tau)}} dt$. The geodesic holds that $\gamma^* = \arg\min_\gamma L(\gamma)$, such that $\gamma(0) = \boldsymbol{x}, \gamma(1) = \boldsymbol{y}$, and $\left\| \frac{d}{d\tau} \gamma(\tau) \right\|_{\gamma(\tau)} = 1$. By the means of the geodesic, the distance between $\mathbf{x}, \mathbf{y} \in \mathcal{Q}_\beta^{s,t}$ is defined as the arc length of geodesic $\gamma(\tau)$.

**Exponential and logarithmic maps** The connections between manifolds and *tangent* space are established by the differentiable exponential map and logarithmic map. The exponential map at $\mathbf{x}$ is defined as $\exp_\mathbf{x}(\boldsymbol{\xi}) = \gamma(1)$, which gives a way to project a vector $\boldsymbol{\xi} \in \mathcal{T}_\mathbf{x}\mathcal{M}$ to a point $\exp_\mathbf{x}(\boldsymbol{\xi}) \in \mathcal{M}$ on the manifold. The logarithmic map $\log_\mathbf{x} : \mathcal{M} \to \mathcal{T}_\mathbf{x}\mathcal{M}$ is defined as the inverse of the exponential map (i.e. $\log_\mathbf{x} = \exp_\mathbf{x}^{-1}$). Note that since $\mathcal{Q}_\beta^{s,t}$ is a geodesically complete manifold, the domain of the exponential map $\mathcal{D}_x$ is hence defined on the entire tangent space, i.e. $\mathcal{D}_x = \mathcal{T}_\mathbf{x}\mathcal{Q}_\beta^{s,t}$. However, as we will explain later, the logarithmic map $\log_\mathbf{x}(\mathbf{y})$ is only defined when there exists a a length-minimizing geodesic between $\mathbf{x}, \mathbf{y} \in \mathcal{Q}_\beta^{s,t}$. More details can be found in the Appendix C.

**Geodesical connectedness** A pseudo-Riemannian manifold $\mathcal{M}$ is *connected* iff any two points of $\mathcal{M}$ can be joined by a piecewise (broken) geodesic with each piece being a smooth geodesic. The manifold is *geodesically connected* (or *g-connected*) iff any two points can be smoothly connected by a geodesic, where the two points are called *g-connected*, otherwise called *g-disconnected*. Different from Riemannian manifolds in which the geodesical completeness implies the g-connectedness (Hopf–Rinow theorem [28]), pseudo-hyperboloid is a geodesically complete but not *g-connected* manifold where there exist points that cannot be smoothly connected by a geodesic [29]. Formally, in the pseudo-hyperboloid, two points $\mathbf{x}, \mathbf{y} \in \mathcal{Q}_\beta^{s,t}$ are *g-connected* iff $\langle \mathbf{x}, \mathbf{y} \rangle_t < |\beta|$. The set of *g-connected* points of $\mathbf{x} \in \mathcal{Q}_\beta^{s,t}$ is denoted as its *normal neighborhood* $\mathcal{U}_\mathbf{x} =$

3

$\left\{ \mathbf{y} \in \mathcal{Q}_\beta^{s,t} : \langle \mathbf{x}, \mathbf{y} \rangle_t < |\beta| \right\}$. For *g-disconnected* points $\mathbf{x}, \mathbf{y} \in \mathcal{Q}_\beta^{s,t}$, there does not exist a tangent vector $\boldsymbol{\xi}$ such that $\mathbf{y} = \exp_{\mathbf{x}}^\beta(\boldsymbol{\xi})$, which implies that its inverse $\log_{\mathbf{x}}^\beta(\cdot)$ is only defined in the *normal neighborhood* of $\mathbf{x}$. In a nutshell, the geodesic tools for the *g-disconnected* cases are not well-defined, making it impossible to define corresponding vector operations.

# 3  Pseudo-Riemannian GCNs

In this section, we first describe how to tackle the *g-disconnectedness* in pseudo-Riemannian manifolds. Then we present the pseudo-Riemannian GCNs based on the proposed geodesic tools.

## 3.1  Diffeomorphic geodesic tools

One standard way to tackle the *g-disconnectedness* in differential geometry is to introduce diffeomorphic manifolds in which the operations are well-defined. A diffeomorphic manifold can be derived from a diffeomorphism, defined as follows.

**Definition 1** (Diffeomorphism [26]). *Given two manifolds $\mathcal{M}$ and $\mathcal{M}'$, a smooth map $\psi : \mathcal{M} \to \mathcal{M}'$ is called a diffeomorphism if $\psi$ is bijective and its inverse $\psi^{-1}$ is smooth as well. If a diffeomorphism between $\mathcal{M}$ and $\mathcal{M}'$ exists, we call them diffeomorphic and write $\mathcal{M} \simeq \mathcal{M}'$.*

For pseudo-Riemannian manifolds, the following diffeomorphism [23] decomposes pseudo-hyperboloid into the product manifolds of an unit sphere and the Euclidean space.

**Theorem 1** (Theorem 4.1 in [23]). *For any point $\mathbf{x} \in \mathcal{Q}_\beta^{s,t}$, there exists a diffeomorphism $\psi : \mathcal{Q}_\beta^{s,t} \to \mathbb{S}_1^t \times \mathbb{R}^s$ that maps $\mathbf{x}$ into the product manifolds of an unit sphere and the Euclidean space.*

The diffeomorphism is given in the Appendix D.1. In light of this, we introduce a new diffeomorphism that maps $\mathbf{x}$ to the product manifolds of sphere with curvature $-1/\beta$ and the Euclidean space.

**Theorem 2.** *For any point $\mathbf{x} \in \mathcal{Q}_\beta^{s,t}$, there exists a diffeomorphism $\psi : \mathcal{Q}_\beta^{s,t} \to \mathbb{S}_{-\beta}^t \times \mathbb{R}^s$ that maps $\mathbf{x}$ into the product manifolds of a sphere and the Euclidean space (proof in the Appendix D.2).*

Compared with Theorem 1, this diffeomorphism preserves the curvatures in the diffeomorphic components, making it satisfy some geometric properties, e.g. the mapped point $\mathbf{x}_t \in \mathbb{S}_{-\beta}^t$ still lies on the surface of the pseudo-hyperboloid, making moving the tangent vectors from the pseudo-hyperboloid to the diffeomorphic manifold easy as we explained later. We call $\psi$ as the spherical projection.

**Exponential and logarithmic maps.** Considering that pseudo-hyperboloid $\mathcal{Q}_\beta^{s,t}$ is *g-disconnected*, we propose to transfer the *logmap* and *expmap* into the diffeomorphic manifold $\psi : \mathcal{Q}_\beta^{s,t} \to \mathbb{S}_{-\beta}^t \times \mathbb{R}^s$, since the product manifold $\mathbb{S}_{-\beta}^t \times \mathbb{R}^s$ is *g-connected*. To map tangent vectors between tangent space of $\mathcal{Q}_\beta^{s,t}$ and $\mathbb{S}_{-\beta}^t \times \mathbb{R}^s$, we exploit *pushforward* that induce a linear approximation of smooth maps on tangent spaces.

**Definition 2** (Pushforward). *Suppose that $\psi : \mathcal{M} \to \mathcal{M}'$ is a smooth map, then the differential of $\psi : d\psi$ at point $\mathbf{x}$ is a linear map from the tangent space of $\mathcal{M}$ at $\mathbf{x}$ to the tangent space of $\mathcal{M}'$ at $\psi(\mathbf{x})$. Namely, $d\psi : \mathcal{T}_x \mathcal{M} \to \mathcal{T}_{\psi(x)} \mathcal{M}'$*

Intuitively, *pushforward* can be used to *push* tangent vectors on $\mathcal{T}_x \mathcal{Q}_\beta^{s,t}$ forward to tangent vectors on $\mathcal{T}_{\psi(x)} \mathbb{S}_{-\beta}^t \times \mathbb{R}^s$. Based on this, the new *logmap* and its inverse *expmap* can be defined by Eq. (1).

$$\widehat{\log}_{\mathcal{Q}_\beta^{s,t}}(\mathbf{x}) = \psi^{-1}(\log_{\mathbb{S}_{-\beta}^t \times \mathbb{R}^s}(\psi(\mathbf{x}))), \quad \widehat{\exp}_{\mathcal{Q}_\beta^{s,t}}(\boldsymbol{\xi}) = \psi^{-1}(\exp_{\mathbb{S}_{-\beta}^t \times \mathbb{R}^s}(\psi(\boldsymbol{\xi}))), \quad (1)$$

where $\psi(\cdot)$ is the spherical projection and $\psi^{-1}(\cdot)$ is the inverse. The mapping of tangent vectors is achieved by *pushforward* operations. The operations $\log_{\mathbb{S}_{-\beta}^t \times \mathbb{R}^s}(\cdot)$ and $\exp_{\mathbb{S}_{-\beta}^t \times \mathbb{R}^s}(\cdot)$ in the product manifolds can be defined as the concatenation of corresponding operations in different components.

$$\log_{\mathbb{S}_{-\beta}^t \times \mathbb{R}^s}(\mathbf{x}') = \log_{\mathbb{S}_{-\beta}^t}(\mathbf{x}_t') \,\|\, \log_{\mathbb{R}^s}(\mathbf{x}_s'), \quad \exp_{\mathbb{S}_{-\beta}^t \times \mathbb{R}^s}(\boldsymbol{\xi}) = \exp_{\mathbb{S}_{-\beta}^t}(\boldsymbol{\xi}_t) \,\|\, \exp_{\mathbb{R}^s}(\boldsymbol{\xi}_s), \quad (2)$$

where $\|$ denotes the concatenation, $\mathbf{x}' = \psi_{\mathbb{S}}(\mathbf{x})$ consists of spherical features $\mathbf{x}_t' \in \mathbb{S}_{-\beta}^t$ and Euclidean features $\mathbf{x}_s' \in \mathbb{R}^s$. $\boldsymbol{\xi}$ is the tangent vector induced by $\mathbf{x}$ on $\mathcal{Q}_\beta^{s,t}$.

We choose points where space dimension $\mathbf{s} = \mathbf{0}$ as the reference points due to the following property.

4

**Theorem 3.** *For any reference point* $\mathbf{x} = \begin{pmatrix} \mathbf{t} \\ \mathbf{s} \end{pmatrix} \in \mathcal{Q}_\beta^{s,t}$ *with space dimension* $\mathbf{s} = \mathbf{0}$*, the induced tangent space of* $\mathcal{Q}_\beta^{s,t}$ *is equal to the tangent space of its diffeomorphic manifold* $\mathbb{S}_{-\beta}^t \times \mathbb{R}^s$*, namely,* $\mathcal{T}_\mathbf{x}(\mathbb{S}_{-\beta}^t \times \mathbb{R}^s) = \mathcal{T}_\mathbf{x}\mathcal{Q}_\beta^{s,t}$*. (proof in the Appendix D.3).*

The intuition of proof is that if space dimension $\mathbf{s} = \mathbf{0}$, the pushforward (differential) function just influences time dimension, for which the mapping is just an identity function (see Appendix D.2). In this way, although we transfer *logmap* and *expmap* to the diffeomorphic manifold $\mathbb{S}_{-\beta}^t \times \mathbb{R}^s$, the diffeomorphic operations $\widehat{\log}_\mathbf{x}(\cdot)$ and $\widehat{\exp}_\mathbf{x}(\cdot)$ are still bijective functions from the pseudo-hyperboloid to the tangent space of the manifold itself. Hence, our final operations are actually still defined in the tangent space of the pseudo-hyperboloid. Note that such property only holds when our Theorem 2 is applied and the special reference points with space dimension $\mathbf{s} = \mathbf{0}$ are chosen.

By leveraging the new *logmap* and *expmap*, we further formulate the diffeomorphic version of tangential operations as follows.

**Tangential operations.** For function $f : \mathbb{R}^d \to \mathbb{R}^{d'}$, the pseudo-hyperboloid version $f^\otimes : \mathcal{Q}_\beta^{s,t} \to \mathcal{Q}_\beta^{s',t'}$ with $s + t = d$ and $s' + t' = d'$ can be defined by the means of $\widehat{\log}_\mathbf{x}^\beta(\cdot)$ and $\widehat{\exp}_\mathbf{x}^\beta(\cdot)$ as Eq. (3).

$$f^\otimes(\cdot) := \widehat{\exp}_\mathbf{x}^\beta \left( f \left( \widehat{\log}_\mathbf{x}^\beta(\cdot) \right) \right), \tag{3}$$

where $\mathbf{x}$ is the reference point. Note that this function is a morphism (i.e. $(f \circ g)^\otimes = f^\otimes \circ g^\otimes$) and direction preserving (i.e. $f^\otimes(\cdot)/\|f^\otimes(\cdot)\| = f(\cdot)/\|f(\cdot)\|$) [14], making it a natural way to define pseudo-hyperboloid version of vector operations such like scalar multiplication, matrix-vector multiplication, tangential aggregation and point-wise non-linearity and so on.

**Parallel transport.** Parallel transport is the generalization of Euclidean translation into manifolds. Formally, for any two points $\mathbf{x}$ and $\mathbf{y}$ connected by a geodesic, parallel transport $P_{\mathbf{x}\to\mathbf{y}}^\beta(\boldsymbol{\xi}) : \mathcal{T}_\mathbf{x}\mathcal{M} \to \mathcal{T}_\mathbf{y}\mathcal{M}$ is an isomorphism between two tangent spaces by moving one tangent vector $\boldsymbol{\zeta} \in \mathcal{T}_x\mathcal{M}$ with tangent direction $\boldsymbol{\xi} \in \mathcal{T}_x\mathcal{M}$ to another tangent space $\mathcal{T}_\mathbf{y}\mathcal{M}$. The parallel transport in pseudo-hyperboloid can be defined as the combination of Riemannian parallel transport [30]. However, the parallel transport has not been defined when there does not exist a geodesic between $\mathbf{x}$ and $\mathbf{y}$. i.e., the tangent vector $\boldsymbol{\zeta}$ induced by $\mathbf{x}$ can not be transported to the tangent space of points outside of the normal neighborhood $\mathcal{U}_\mathbf{x}$. Intuitively, the normal neighborhoods satisfy the following property.

**Theorem 4.** *For any point* $\mathbf{x} \in \mathcal{Q}_\beta^{s,t}$*, the union of the normal neighborhood of* $\mathbf{x}$ *and the normal neighborhood of its antipodal point* $-\mathbf{x}$ *cover the entire manifold. Namely,* $\mathcal{U}_\mathbf{x} \cup \mathcal{U}_{-\mathbf{x}} = \mathcal{Q}_\beta^{s,t}$ *(proof in the Appendix D.4).*

This theorem ensures that if a point $\mathbf{y} \notin \mathcal{U}_\mathbf{x}$, its antipodal point $-\mathbf{y} \in \mathcal{U}_\mathbf{x}$. Besides, $\mathcal{T}_\mathbf{y}\mathcal{M}$ is parallel to $\mathcal{T}_{-\mathbf{y}}\mathcal{M}$. Hence, $P_{\mathbf{x}\to\mathbf{y}}^\beta$ can be alternatively defined as $P_{\mathbf{x}\to-\mathbf{y}}^\beta$ for broken points. This result is crucial to define the pseudo-hyperbolic addition, such as bias translation, detailed in section 3.2.

**Broken geodesic distance.** By the means of geodesic, the induced distance between $\mathbf{x}$ and $\mathbf{y}$ in pseudo-hyperboloid is defined as the arc length of geodesic $\gamma(\tau)$, given by $d_\gamma(\mathbf{x}, \mathbf{y}) = \sqrt{\|\log_\mathbf{x}(\mathbf{y})\|_t^2}$. For broken cases in which $\log_\mathbf{x}(\mathbf{y})$ is not defined, one approach is to use approximation like [23]. Different from that, we define following closed-form distance, given by Eq. (4).

$$\mathrm{D}_\gamma(\mathbf{x}, \mathbf{y}) = \begin{cases} \mathrm{d}_\gamma(\mathbf{x}, \mathbf{y}), & \text{if } \langle \mathbf{x}, \mathbf{y} \rangle_t < |\beta| \\ \pi\sqrt{|\beta|} + \mathrm{d}_\gamma(\mathbf{x}, -\mathbf{y}), & \text{if } \langle \mathbf{x}, \mathbf{y} \rangle_t \geq |\beta| \end{cases} \tag{4}$$

The intuition is that when $\mathbf{x}, \mathbf{y} \in \mathcal{Q}_\beta^{s,t}$ are *g-disconnected*, we consider the distance as $\mathrm{d}_\gamma(\mathbf{x}, \mathbf{y}) = \mathrm{d}_\gamma(\mathbf{x}, -\mathbf{x}) + \mathrm{d}_\gamma(-\mathbf{x}, \mathbf{y})$ or $\mathrm{d}_\gamma(\mathbf{x}, \mathbf{y}) = \mathrm{d}_\gamma(\mathbf{x}, -\mathbf{y}) + \mathrm{d}_\gamma(-\mathbf{y}, \mathbf{y})$. Since $\mathrm{d}_\gamma(\mathbf{x}, -\mathbf{x}) = \mathrm{d}_\gamma(-\mathbf{y}, \mathbf{y}) = \pi\sqrt{|\beta|}$ is a constant and $\mathrm{d}_\gamma(-\mathbf{x}, \mathbf{y}) = \mathrm{d}_\gamma(\mathbf{x}, -\mathbf{y})$, the distance between broken points can be calculated as $\mathrm{d}_\gamma(\mathbf{x}, \mathbf{y}) = \pi\sqrt{|\beta|} + \mathrm{d}_\gamma(\mathbf{x}, -\mathbf{y})$.

To clarify theoretical contributions, our Theorem 2 is nessasary for our Theorem 3 while Theorem 3 is nessasary for transforming the GCN operations directly into the tangent space of the pseudo-hyperboloid. Besides, we are the first to formulate the diffeomorphic *expmap*, *logmap* and tangential

5

operations of pseudo-hyperboloid to avoid broken cases. The theoretical properties of parallel transport and geodesic distance are discussed in the literature [23, 30]. However, we re-formulate parallel transport with Theorem 4 to avoid broken issues and propose a new distance measure using the broken geodesic (Eq.4 ), which is different from the approximated distance in [23].

## 3.2 Model architecture

GCNs can be interpreted as performing neighborhood aggregation after a linear transformation on node features of each layer. We present pseudo-Riemannian GCNs ($\mathcal{Q}$-GCN) by deriving corresponding operations with the developed geodesic tools in the $\mathcal{Q}_\beta^{s,t}$.

**Feature initialization.** We first map the features from Euclidean space to pseudo-hyperboloid, considering that the input features of nodes usually live in Euclidean space. Following the feature transformation from Euclidean space to pseudo-hyperboloid in [23], we initialize the node features by performing a differentiable mapping $\varphi : \mathbb{R}_*^{t+1} \times \mathbb{R}^s \to \mathcal{Q}_\beta^{s,t}$ that can be implemented by a double projection [23] based on Theorem 2, i.e. $\varphi = \psi^{-1} \circ \psi$. The intuition is that we first map the Euclidean features into diffeomorphic manifolds $\mathbb{S}_{-\beta}^t \times \mathbb{R}^s$ via $\psi(\cdot)$, and then map them into the pseudo-hyperboloid $\mathcal{Q}_\beta^{s,t}$ via $\psi^{-1}(\cdot)$, where the mapping functions are given by Eq. (5).

$$\psi(\mathbf{x}) = \begin{pmatrix} \sqrt{|\beta|}\frac{\mathbf{t}}{\|\mathbf{t}\|} \\ \mathbf{s} \end{pmatrix} \quad , \quad \psi^{-1}(\mathbf{z}) = \begin{pmatrix} \frac{\sqrt{|\beta|+\|\mathbf{v}\|^2}}{\sqrt{|\beta|}}\mathbf{u} \\ \mathbf{v} \end{pmatrix}, \tag{5}$$

where $\mathbf{x} = (\mathbf{t}, \mathbf{s})^\top \in \mathcal{Q}_\beta^{s,t}$ with $\mathbf{t} \in \mathbb{R}_*^t$ and $\mathbf{s} \in \mathbb{R}^s$. $\mathbf{z} = (\mathbf{u}, \mathbf{v})^\top \in \mathbb{S}_{-\beta}^t \times \mathbb{R}^s$ with $\mathbf{u} \in \mathbb{S}_{-\beta}^t$ and $\mathbf{v} \in \mathbb{R}^s$.

**Tangential aggregation.** The linear combination of neighborhood features is lifted to the tangent space, which is an intrinsic operation in differential manifolds [31, 15]. Specifically, $\mathcal{Q}$-GCN aggregates neighbours' embeddings in the tangent space of the reference point $\mathbf{o}$ before passing through a tangential activation function, and then projects the updated representation back to the manifold. Formally, at each layer $\ell$, the updated features of each node $i$ are defined as Eq. (6).

$$\mathbf{h}_i^{\ell+1} = \widehat{\exp}_\mathbf{o}^{\beta_{\ell+1}} \left( \sigma \left( \sum_{j \in \mathcal{N}(i) \cup \{i\}} \widehat{\log}_\mathbf{o}^{\beta_\ell} \left( W^\ell \otimes^{\beta_\ell} \mathbf{h}_j^\ell \oplus^{\beta_\ell} \mathbf{b}^\ell \right) \right) \right), \tag{6}$$

where $\sigma(\cdot)$ is the activation function, $\beta_\ell$ and $\beta_{\ell+1}$ are two layer-wise curvatures, $\mathcal{N}(i)$ denotes the one-hop neighborhoods of node $i$, and the $\otimes, \oplus$ denote two basic operations, i.e. tangential transformation and bias translation, respectively.

**Tangential transformation.** We perform Euclidean transformations on the tangent space by leveraging the *expmap* and *logmap* in Eq. (1). Specifically, we first project the hidden feature into the tangent space of *south pole* $\mathbf{o} = [|\beta|, 0, , ..., 0]$ using *logmap* and then perform Euclidean matrix multiplication. Afterwards, the transformed features are mapped back to the manifold using *expmap*.

Formally, at each layer $\ell$, the tangential transformation is given by $W^\ell \otimes^\beta \mathbf{h}^\ell := \widehat{\exp}_\mathbf{o}^\beta (W^\ell \widehat{\log}_\mathbf{o}^\beta (\mathbf{h}^\ell))$, where $\otimes^\beta$ denotes the pseudo-hyperboloid tangential multiplication, and $W^\ell \in \mathbb{R}^{d' \times d}$ denotes the layer-wise learnable matrix in Euclidean space.

**Bias translation.** It is noteworthy that simply stacking multiple layers of the tangential transformation would collapse the composition [31, 14], i.e. $\exp_\mathbf{o}^\beta ...(W^1 \log_\mathbf{o}^\beta(\exp_\mathbf{o}^\beta(W^0 \log_\mathbf{o}^\beta(x)))) = \exp_\mathbf{o}^\beta(W^0 \times W^1 \times ... \times \log_\mathbf{o}^\beta(x))$, which means that these multiplications can simply be performed in Euclidean space except the first *logmap* and last *expmap*. To avoid model collapsing , we perform bias translation after the tangential transformation. By the means of pseudo-hyperboloid *parallel transport*, the bias translation can be performed by parallel transporting a tangent vector $\mathbf{b}^\ell \in \mathcal{T}_\mathbf{o}\mathcal{Q}_\beta^{s,t}$ to the tangent space of the point of interest. Finally, the transported tangent vector is mapped back to the manifold with *expmap*. Considering that $\widehat{\exp}(\cdot)$ is only defined at point $\mathbf{x} \in \mathcal{Q}_\beta^{s,t}$ with the space dimension $\mathbf{x}_s = \mathbf{0}$, we perform the original $\exp_{\mathcal{Q}_\beta^{s,t}}(\cdot)$ at the point of interest. The bias translation is formally given by:

$$\widetilde{\mathbf{h}}^\ell \oplus^\beta \mathbf{b}^\ell := \begin{cases} \exp_{\widetilde{\mathbf{h}}^\ell}^\beta \left( P_{\mathbf{o} \to \widetilde{\mathbf{h}}^\ell}^\beta \left( \mathbf{b}^\ell \right) \right), & \text{if } \langle \mathbf{o}, \widetilde{\mathbf{h}}^\ell \rangle_t < |\beta| \\ -\exp_{-\widetilde{\mathbf{h}}^\ell}^\beta \left( P_{\mathbf{o} \to -\widetilde{\mathbf{h}}^\ell}^\beta \left( \mathbf{b}^\ell \right) \right), & \text{if } \langle \mathbf{o}, \widetilde{\mathbf{h}}^\ell \rangle_t \geq |\beta| \end{cases} \tag{7}$$

where $\widetilde{\mathbf{h}}^\ell = W^\ell \otimes^\beta \mathbf{h}^\ell$, $\oplus^\beta$ denotes the pseudo-hyperboloid addition. For the broken cases where $\langle \mathbf{o}, \widetilde{\mathbf{h}}^\ell \rangle_t \geq |\beta|$, the parallel transport $P^\beta_{\mathbf{o} \to \widetilde{\mathbf{h}}^\ell}$ is not defined. In this case, we parallel transport $\mathbf{b}^\ell$ to the tangent space of the antipodal point $-\widetilde{\mathbf{h}}^\ell$, and then perform $\exp^\beta_{-\widetilde{\mathbf{h}}^\ell}$ to map it back to the manifold. Note that the case $\langle \mathbf{o}, \widetilde{\mathbf{h}}^\ell \rangle_t = |\beta|$ occurs if and only if $\mathbf{h} = -\mathbf{o}$, in which case $P^\beta_{\mathbf{o} \to -\widetilde{\mathbf{h}}^\ell}\left(\mathbf{b}^\ell\right) = P^\beta_{\mathbf{o} \to -\mathbf{o}}\left(\mathbf{b}^\ell\right) = -\mathbf{b}$.

### 3.3 Model training

Having introduced all the building blocks, $\mathcal{Q}$-GCN stacks multiple pseudo-Riemannian GCN layers and the final embeddings at the last layer can then be used to perform downstream tasks. For graph reconstruction, the objective is to map all nodes into a low-dimensional space such that the connected nodes are closer than unconnected nodes. Following [19, 23], we minimize the loss function $\mathcal{L}(\Theta) = \sum_{(u,v) \in \mathcal{D}} \log \frac{e^{-d(\boldsymbol{u},\boldsymbol{v})}}{\sum_{\boldsymbol{v}' \in \mathcal{E}(u)} e^{-d(\boldsymbol{u},\boldsymbol{v}')}}$ under the set of connected relations $\mathcal{D}$ in the graph, where $\mathcal{E}(u) = \{v | (u,v) \notin D, v \neq u\}$ is the set of negative examples for node $u$, $d(\cdot)$ is the distance function defined in Eq. (4). For node classification, we map the output of the last layer of $\mathcal{Q}$-GCN to the tangent space, and then perform Euclidean multinomial logistic regression. For link prediction, we utilize the Fermi-Dirac decoder [8] to compute probability scores for edges, formally given by $P(e_{uv} \in \mathcal{E} | \Theta) = \frac{1}{e^{(d(\mathbf{u},\mathbf{v})-r)/t}+1}$, where $r$ and $t$ are hyperparameters, $d(\mathbf{u}, \mathbf{v})$ is the distance function in the embedding space. We then train $\mathcal{Q}$-GCN by minimizing the cross-entropy loss using negative sampling.

**Optimization.** Although the model is built in $\mathcal{Q}^{s,t}_\beta$, the trainable parameters are all defined in Euclidean space through the diffeomorphic mappings. Following the standard tangential optimization strategy [31], the parameters can be optimized via Euclidean optimization by applying layer-wise diffeomorphic *expmap* and *logmap*. One optional strategy is to use dedicated optimization like [23], which we left for our future work.

**Complexity analysis.** The time complexity is the same as a vanilla GCN given by $O(|V|dd'+|E|d')$, where $|V|$ and $|E|$ are the number of nodes and edges, $d$ and $d'$ are the dimension of input and hidden features. The computation can be parallelized across all nodes. Similar to other non-Euclidean GCNs [31, 32, 16], the mapping from manifolds to the tangent space consume additional computation resources, compared with Euclidean GCNs, which is within the acceptable limits.

## 4 Experiments

We evaluate the effectiveness of $\mathcal{Q}$-GCN on graph reconstruction, node classification and link prediction. Firstly, we study the geometric properties of the used datasets including the graph sectional curvature [19] and the $\delta$-hyperbolicity [7]. Fig. 4 in the Appendix shows the histograms of sectional curvature and the mean sectional curvature for all datasets. It can be seen that all datasets have both positive and negative sectional curvatures, showcasing that all graphs contain mixed graph topologies. To further analyze the degree of the hierarchy, we apply $\delta$-hyperbolicity to identify the tree-likeness, as shown in Table 9 in the Appendix. We conjecture that the datasets with positive graph sectional curvature or larger $\delta$-hyperbolicity should be suitable for pseudo-hyperboloid with a smaller time dimension, while datasets with negative graph sectional curvature or smaller $\delta$-hyperbolicity should be aligned well with pseudo-hyperboloid with a larger time dimension.

### 4.1 Graph reconstruction

**Datasets and baselines.** We benchmark graph reconstruction on four real-world graphs including 1) Web-Edu [33]: a web network consisting of the $.edu$ domain; 2) Power [34]: a power grid distribution network with backbone structure; 3) Bio-Worm [35]: a worms gene network; 4) Facebook [36]: a dense social network from Facebook. We compare our method with Euclidean GCN [2], hyperbolic GCN (HGCN) [31], spherical GCN, and product manifold GCNs ($\kappa$-GCN) [32] with three signatures (i.e. $\mathbb{H}^5 \times \mathbb{H}^5$, $\mathbb{H}^5 \times \mathbb{S}^5$ and $\mathbb{S}^5 \times \mathbb{S}^5$). Besides, five variants of our model are implemented with different time dimension in $[1, 3, 5, 7, 10]$ for comparison.

Table 2: ROC AUC (%) for Link Prediction (LP) and F1 score for Node Classification (NC).

| Dataset $\delta$-hyperbolicity | Airport 1.0 | | Pubmed 3.5 | | CiteSeer 4.5 | | Cora 11.0 | |
|---|---|---|---|---|---|---|---|---|
| Method | LP | NC | LP | NC | LP | NC | LP | NC |
| GCN | 89.24±0.21 | 81.54±0.60 | 91.31±1.68 | 79.30±0.60 | 85.48±1.75 | 72.27±0.64 | 88.52±0.85 | 81.90±0.41 |
| GAT | 90.35±0.30 | 81.55±0.53 | 87.45±0.00 | 78.30±0.00 | 87.24±0.00 | 71.10±0.00 | 85.73±0.01 | 83.05±0.08 |
| SAGE | 89.86±0.52 | 82.79±0.17 | 90.70±0.07 | 77.30±0.09 | 90.71±0.20 | 69.20±0.10 | 87.52±0.22 | 74.90±0.07 |
| SGC | 89.80±0.34 | 80.69±0.23 | 90.54±0.07 | 78.60±0.30 | 89.61±0.23 | 71.60±0.03 | 89.42±0.11 | 81.60±0.43 |
| HGCN ($\mathbb{H}^{16}$) | 96.03±0.26 | 90.57±0.36 | 96.08±0.21 | 80.50±1.23 | 96.31±0.41 | 68.90±0.63 | 91.62±0.33 | 79.90±0.18 |
| $\kappa$-GCN ($\mathbb{H}^{16}$) | 96.35±0.62 | 87.92±1.33 | 96.60±0.32 | 77.96±0.36 | 95.34±0.16 | 73.25±0.51 | 94.04±0.34 | 79.80±0.50 |
| $\kappa$-GCN ($\mathbb{S}^{16}$) | 90.38±0.32 | 81.94±0.58 | 94.84±0.13 | 78.80±0.49 | 95.79±0.24 | 72.13±0.51 | 93.20±0.48 | 81.08±1.45 |
| $\kappa$-GCN ($\mathbb{H}^8 \times \mathbb{S}^8$) | 93.10±0.49 | 81.93±0.45 | 94.89±0.19 | 79.20±0.65 | 93.44±0.31 | 73.05±0.59 | 92.22±0.48 | 79.30±0.81 |
| $\mathcal{Q}$-GCN ($\mathcal{Q}^{15,1}$) | 96.30±0.22 | 89.72±0.52 | 95.42±0.22 | 80.50±0.26 | 94.76±1.49 | 72.67±0.76 | 93.14±0.30 | 80.57±0.20 |
| $\mathcal{Q}$-GCN ($\mathcal{Q}^{14,2}$) | 94.37±0.44 | 84.40±0.35 | 96.86±0.37 | 81.34±1.54 | 94.78±0.17 | 73.43±0.58 | 93.41±0.57 | 81.62±0.21 |
| $\mathcal{Q}$-GCN ($\mathcal{Q}^{13,3}$) | 92.53±0.17 | 82.38±1.53 | 96.20±0.34 | 80.94±0.45 | 94.54±0.16 | 74.13±1.41 | 93.56±0.18 | 79.91±0.42 |
| $\mathcal{Q}$-GCN ($\mathcal{Q}^{2,14}$) | 90.03±0.12 | 81.14±1.32 | 94.30±1.09 | 78.40±0.39 | 94.80±0.08 | 72.72±0.47 | 94.17±0.38 | 83.10±0.35 |
| $\mathcal{Q}$-GCN ($\mathcal{Q}^{1,15}$) | 89.07±0.58 | 81.24±0.34 | 94.66±0.18 | 78.11±1.38 | 97.01±0.30 | 73.19±1.58 | 94.81±0.27 | 83.72±0.43 |
| $\mathcal{Q}$-GCN ($\mathcal{Q}^{0,16}$) | 89.01±0.61 | 80.91±0.65 | 94.49±0.28 | 77.90±0.80 | 96.21±0.38 | 72.54±0.27 | 95.16±1.25 | 82.51±0.32 |

**Experimental settings.** Following [19, 23, 32], we use one-hot embeddings as initial node features. To avoid the time dimensions being $\mathbf{0}$, we uniformly perturb each dimension with a small random value in the interval $[-\epsilon, \epsilon]$, where $\epsilon = 0.02$ in practice. In addition, the same 10-dimensional embedding and 2 hidden layers are used for all baselines to ensure a fair comparison. The learning rate is set to 0.01, the learning rate of curvature is set to 0.0001. $\mathcal{Q}$-GCN is implemented with the Adam optimizer. We repeat the experiments 10 times via different random seeds influencing weight initialization and data batching.

Table 1: The graph reconstruction results in mAP (%), top three results are highlighted. Standard deviations are relatively small (in range $[0, 1.2 \times 10^{-2}]$) and are omitted.

| Model | Web-Edu | Power | Bio-Worm | Facebook |
|---|---|---|---|---|
| Curvature | -0.6 | -0.3 | 0.0 | 0.1 |
| GCN ($\mathbb{E}^{10}$) | 83.66 | 86.61 | 90.19 | 81.73 |
| HGCN ($\mathbb{H}^{10}$) | 88.33 | 93.80 | 93.12 | 83.40 |
| GCN ($\mathbb{S}^{10}$) | 82.72 | 92.73 | 88.98 | 81.04 |
| $\kappa$-GCN ($\mathbb{H}^5 \times \mathbb{H}^5$) | 89.21 | 94.40 | 94.00 | 84.94 |
| $\kappa$-GCN ($\mathbb{S}^5 \times \mathbb{S}^5$) | 86.70 | 94.58 | 90.36 | 84.56 |
| $\kappa$-GCN ($\mathbb{H}^5 \times \mathbb{S}^5$) | 87.96 | 95.82 | 94.74 | 87.73 |
| $\mathcal{Q}$-GCN ($\mathcal{Q}^{9,1}$) | 87.03 | 94.35 | 92.83 | 81.60 |
| $\mathcal{Q}$-GCN ($\mathcal{Q}^{7,3}$) | 99.67 | 100.00 | 97.23 | 87.74 |
| $\mathcal{Q}$-GCN ($\mathcal{Q}^{5,5}$) | 98.49 | 100.00 | 95.75 | 87.03 |
| $\mathcal{Q}$-GCN ($\mathcal{Q}^{3,7}$) | 97.31 | 95.08 | 90.14 | 91.75 |
| $\mathcal{Q}$-GCN ($\mathcal{Q}^{0,10}$) | 82.57 | 94.20 | 88.67 | 83.81 |

**Results.** Table 1 shows the mean average precision (mAP) [19] results of graph reconstruction on four datasets. It shows that $\mathcal{Q}$-GCN achieves the best performance across all benchmarks compared with both Riemannian space and product manifolds. We observe that by setting proper signatures, the product spaces perform better than a single geometry. It is consistent with our statement that the expression power of a single view geometry is limited. Specifically, all the top three results are achieved by $\mathcal{Q}$-GCN, with one exception on Power where $\mathbb{H}^5 \times \mathbb{S}^5$ achieved the third-best performance. More precisely, for datasets that have smaller graph sectional curvature like Web-Edu, Power and Bio-Worm, $\mathcal{Q}^{7,3}$ perform the best, while $\mathcal{Q}^{3,7}$ perform the best on Facebook with positive sectional curvature. We conjecture that the number of time dimensions controls the geometry of the pseudo-hyperboloid. We find that the graphs with more hierarchical structures are inclined to be embedded with fewer time dimensions. By analyzing the sectional curvature in Fig. 4, we find that this makes sense as the mean sectional curvature of Power, Bio-Wormnet and Web-Edu are negative while it is negative for Facebook. Such results give us an intuition to determine the best time dimension based on the geometric properties of graphs.

## 4.2 Node classification and link prediction

**Datasets and baselines.** We consider four benchmark datasets: Airport, Pubmed, Citeseer and Cora, where Airport is airline networks, Pubmed, Citeseer and Cora are three citation networks. We observe that the graph sectional curvatures of the four datasets are consistently negative without significant differences in Fig. 4, hence we report the additional $\delta$-hyperbolicity for comparison in Table 2. GCN [2], GAT [3], SAGE [37] and SGC [4] are used as Euclidean GCN counterparts. For non-Euclidean GCN baselines, we compare HGCN [31] and $\kappa$-GCN [32] with its three variants as

Table 3: F1 score for node classification of MLP, HNN and $\mathcal{Q}$-NN on Pubmed, Citeseer and Cora.

| Method | Pubmed | CiteSeer | Cora |
|---|---|---|---|
| MLP | 72.30±0.30 | 60.22±0.42 | 55.80±0.08 |
| HNN | 74.60±0.40 | 59.92±0.87 | 59.60±0.09 |
| $\mathcal{Q}$-NN ($\mathcal{Q}^{15,1}$) | 74.31±0.33 | 59.33±0.35 | 60.38±0.56 |
| $\mathcal{Q}$-NN ($\mathcal{Q}^{14,2}$) | **76.26±0.31** | **64.33±0.35** | 62.77±0.30 |
| $\mathcal{Q}$-NN ($\mathcal{Q}^{13,3}$) | 75.85±0.79 | 63.65±0.57 | 59.04±0.45 |
| $\mathcal{Q}$-NN ($\mathcal{Q}^{2,14}$) | 74.44±0.68 | 60.48±0.29 | 63.85±0.22 |
| $\mathcal{Q}$-NN ($\mathcal{Q}^{1,15}$) | 73.44±0.28 | 60.33±0.40 | **64.85±0.24** |
| $\mathcal{Q}$-NN ($\mathcal{Q}^{0,16}$) | 73.31±0.17 | 61.05±0.22 | 63.96±0.41 |

Table 4: The running time (sec) of graph reconstruction on Web-Edu and Facebook.

| Manifolds | Web-Edu | Facebook |
|---|---|---|
| GCN ($\mathbb{E}^{10}$) | 2284 | 5456 |
| Prod-GCN ($\mathbb{H}^5 \times \mathbb{S}^5$) | 4336 | 10338 |
| $\mathcal{Q}$-GCN ($\mathcal{Q}^{9,1}$) | 2769 | 6981 |
| $\mathcal{Q}$-GCN ($\mathcal{Q}^{7,3}$) | 3363 | 6303 |
| $\mathcal{Q}$-GCN ($\mathcal{Q}^{5,5}$) | 3620 | 7142 |
| $\mathcal{Q}$-GCN ($\mathcal{Q}^{3,7}$) | 3685 | 7512 |
| $\mathcal{Q}$-GCN ($\mathcal{Q}^{1,9}$) | 3532 | 7980 |
| $\mathcal{Q}$-GCN ($\mathcal{Q}^{0,10}$) | 2778 | 7037 |

explained before. For $\mathcal{Q}$-GCN, we empirically set the time dimension as $[1, 2, 3, 14, 15, 16]$ as six variants since these settings best reflect the geometric properties of hyperbolic and spherical space, respectively.

**Experimental settings.** For node classification, we use the same dataset split as [38] for citation datasets, where 20 nodes per class are used for training, and 500 nodes are used for validation and 1000 nodes are used for testing. For Airport, we split the dataset into $70/15/15$. For link prediction, the edges are split into $85/5/10$ percent for training, validation and testing for all datasets. To ensure a fair comparison, we set the same 16-dimension hidden embedding, 0.01 initial learning rate and 0.0001 learning rate for curvature. The optimal regularization with weight decay, dropout rate, the number of layers and activation functions are obtained by grid search for each method. We report the mean accuracy over 10 random seeds influencing weight initialization and batching sequence.

**Results.** Table 2 shows the averaged ROC AUC for link prediction, and F1 score for node classification. As we can see from the $\delta$-hyperbolicity, Airport and Pubmed are more hierarchical than CiteSeer and Cora. For Airport and Pubmed with dominating hierarchical properties (lower $\delta$), $\mathcal{Q}$-GCNs with fewer time dimensions achieve the results on par with hyperbolic space based methods such as HGCN [31], $\kappa$-GCN ($\mathbb{H}^{16}$). While for CiteSeer and Cora with less tree-like properties (higher $\delta$), $\mathcal{Q}$-GCNs achieve the state-of-the-art results, showcasing the flexibility of our model to embed complex graphs with different curvatures. More specifically, $\mathcal{Q}$-GCN with more time dimensions consistently performs best on Cora. While for CiteSeer, albeit $\mathcal{Q}$-GCN achieves the best results, the corresponding best variants are not consistent on both tasks.

### 4.3 Parameter sensitivity and analysis

**Time dimension.** We study the influence of time dimension for graph reconstruction by setting varying number of time dimensions under the condition of $s + t = 10$. Fig. 2 shows that the *time dimension* $t$ acts as a knob for controlling the geometric properties of $\mathcal{Q}_\beta^{s,t}$. The best performance are achieved by neither hyperboloid ($t = 1$) nor sphere cases ($t = 10$), showcasing the advantages of $\mathcal{Q}_\beta^{s,t}$ on representing graphs of mixed topologies. It shows that on Web-Edu, Power and Bio-Worm with smaller mean sectional curvature, after the optimal value is reached at a lower $t$, the performance decrease as $t$ increases. While on Facebook with larger (positive) mean sectional curvature, as $t$ rises, the effect gradually increases until it reaches a peak at a higher $t$. It is consistent with our hypothesis that graphs with



Figure 2: The mAP of graph reconstruction with varying number of time dimensions.

more hierarchical structure are inclined to be embedded in $\mathcal{Q}_\beta^{s,t}$ with smaller $t$, while cyclical data is aligned well with larger $t$. The results give us an intuition to determine the best time dimension based on the geometric properties of graphs.
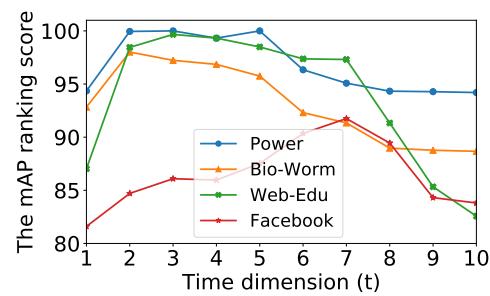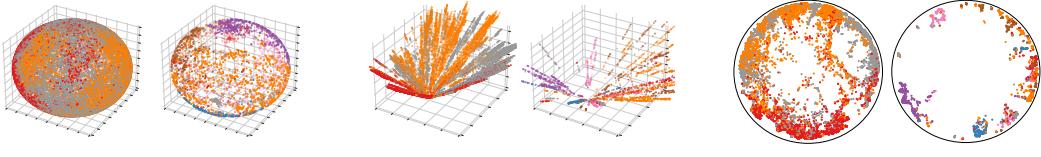
|                        |                           |                             |
| :--------------------: | :-----------------------: | :-------------------------: |
| (a) Spherical projection | (b) Hyperbolic projection (3D) | (c) Hyperbolic projection (disk) |

Figure 3: Visualization of the learned embeddings for link prediction on Pubmed (left) and Cora (right), where the colors denote the class of nodes. We apply (a) spherical projection, (b) hyperbolic projection (3D) and (c) hyperbolic projection (Poincaré disk) on the learned embeddings of $\mathcal{Q}$-GCN to visualize various views of the learned embeddings.

$\mathcal{Q}$-**NN VS $\mathcal{Q}$-GCN.** We also introduce $\mathcal{Q}$-NN, a generalization of MLP into pseudo-Riemannian manifold, defined as multiple layers of $f(\mathbf{x}) = \sigma^{\otimes}(W \otimes^{\beta} \mathbf{x} \oplus^{\beta} \mathbf{b})$, where $\sigma^{\otimes}$ is the tangential activation. Table 3 shows that $\mathcal{Q}$-NN with appropriate time dimension outperforms MLP and HNN on node classification, showcasing the expression power of pseudo-hyperboloid. Furthermore, compared with the results of $\mathcal{Q}$-GCN in Table 2, $\mathcal{Q}$-GCN performs better than $\mathcal{Q}$-NN, suggesting that the benefits of the neighborhood aggregation equipped with the proposed GCN operations.

**Computation efficiency.** We compare the running time of $\mathcal{Q}$-GCN, GCN and Prod-GCN per epoch. Table 4 shows that $\mathcal{Q}$-GCN achieves higher efficiency than Prod-GCN ($\mathbb{H}^5 \times \mathbb{S}^5$). This is mainly owing to that the component $\mathbb{R}$ in our diffeomorphic manifold ($\mathbb{S} \times \mathbb{R}$) runs faster than non-Euclidean components in $\mathbb{H}^5 \times \mathbb{S}^5$. The additional running time mainly comes from the mapping operations and the projection from the time dimensions to $\mathbb{S}$. The running time grows when increasing the number of time dimensions. Overall, albeit slower than Euclidean GCN, the running time of all variants of $\mathcal{Q}$-GCN is smaller than the twice of time in Euclidean GCN, which is within the acceptable limits.

**Visualization.** To visualize the embeddings learned by $\mathcal{Q}$-GCN, we use UMAP tool [2] to project the learned embeddings for Link Prediction on Pubmed and Cora into low-dimensional spherical and hyperbolic spaces. The projections include spherical projection into 3D sphere, hyperbolic projection into 3D plane, and 2D Poincaré disk. As shown in Fig. 3 (a,b), for Pubmed with more hyperbolic structures, the class separability is more significant in hyperbolic projection than that is in spherical projection. While the corresponding result is opposite for less tree-like Cora. Furthermore, Fig. 3 (c) provides a more clear insight of the hierarchy. It shows that there are more hub nodes near the origin of Poincaré disk in Pubmed than in Cora, showcasing the dominating tree-likeness of Pubmed.

## 5   Conclusion

In this paper, we generalize GCNs to pseudo-Riemannian manifolds of constant nonzero curvature with elegant theories of diffeomorphic geometry tools. The proposed $\mathcal{Q}$-GCN have the flexibility to fit complex graphs with mixed curvatures and have shown promising results on graph reconstruction, node classification and link prediction. One limitation might be the choice of time dimension, we provide some insights to decide the best time dimension but this could still be improved, which we left for our future work. The developed geodesic tools are application-agnostic and could be extended to more deep learning methods. We foresee our work would shed light on the direction of non-Euclidean geometric deep learning.

## Acknowledgments

---

[2]https://umap-learn.readthedocs.io/en/latest/index.html

# References

[1] Joan Bruna, Wojciech Zaremba, Arthur Szlam, and Yann LeCun. Spectral networks and locally connected networks on graphs. In Yoshua Bengio and Yann LeCun, editors, *2nd International Conference on Learning Representations, ICLR 2014, Banff, AB, Canada, April 14-16, 2014, Conference Track Proceedings*, 2014.

[2] Thomas N. Kipf and Max Welling. Semi-supervised classification with graph convolutional networks. In *5th International Conference on Learning Representations, ICLR 2017, Toulon, France, April 24-26, 2017, Conference Track Proceedings*. OpenReview.net, 2017.

[3] Petar Velickovic, Guillem Cucurull, Arantxa Casanova, Adriana Romero, Pietro Liò, and Yoshua Bengio. Graph attention networks. In *6th International Conference on Learning Representations, ICLR 2018, Vancouver, BC, Canada, April 30 - May 3, 2018, Conference Track Proceedings*. OpenReview.net, 2018.

[4] Felix Wu, Amauri H. Souza Jr., Tianyi Zhang, Christopher Fifty, Tao Yu, and Kilian Q. Weinberger. Simplifying graph convolutional networks. In Kamalika Chaudhuri and Ruslan Salakhutdinov, editors, *Proceedings of the 36th International Conference on Machine Learning, ICML 2019, 9-15 June 2019, Long Beach, California, USA*, volume 97 of *Proceedings of Machine Learning Research*, pages 6861–6871. PMLR, 2019.

[5] Ke Sun, Jun Wang, Alexandros Kalousis, and Stéphane Marchand-Maillet. Space-time local embeddings. In Corinna Cortes, Neil D. Lawrence, Daniel D. Lee, Masashi Sugiyama, and Roman Garnett, editors, *Advances in Neural Information Processing Systems 28: Annual Conference on Neural Information Processing Systems 2015, December 7-12, 2015, Montreal, Quebec, Canada*, pages 100–108, 2015.

[6] Marián Boguñá, Ivan Bonamassa, Manlio De Domenico, Shlomo Havlin, Dmitri Krioukov, and M Ángeles Serrano. Network geometry. *Nature Reviews Physics*, pages 1–22, 2021.

[7] Mikhael Gromov. Hyperbolic groups. In *Essays in group theory*, pages 75–263. Springer, 1987.

[8] Dmitri Krioukov, Fragkiskos Papadopoulos, Maksim Kitsak, Amin Vahdat, and Marián Boguná. Hyperbolic geometry of complex networks. *Physical Review E*, 82(3):036106, 2010.

[9] Bo Xiong, Michael Cochez, Mojtaba Nayyeri, and Steffen Staab. Hyperbolic embedding inference for structured multi-label prediction. *Advances in Neural Information Processing Systems*, 2022.

[10] Menglin Yang, Zhihao Li, Min Zhou, Jiahong Liu, and Irwin King. Hicf: Hyperbolic informative collaborative filtering. In *Proceedings of the 28th ACM SIGKDD Conference on Knowledge Discovery and Data Mining*, pages 2212–2221, 2022.

[11] Richard C Wilson, Edwin R Hancock, Elżbieta Pekalska, and Robert PW Duin. Spherical and hyperbolic embeddings of data. *IEEE transactions on pattern analysis and machine intelligence*, 36(11):2255–2269, 2014.

[12] Yu Meng, Jiaxin Huang, Guangyuan Wang, Chao Zhang, Honglei Zhuang, Lance M. Kaplan, and Jiawei Han. Spherical text embedding. In Hanna M. Wallach, Hugo Larochelle, Alina Beygelzimer, Florence d'Alché-Buc, Emily B. Fox, and Roman Garnett, editors, *Advances in Neural Information Processing Systems 32: Annual Conference on Neural Information Processing Systems 2019, NeurIPS 2019, December 8-14, 2019, Vancouver, BC, Canada*, pages 8206–8215, 2019.

[13] Michaël Defferrard, Nathanaël Perraudin, Tomasz Kacprzak, and Raphael Sgier. Deepsphere: towards an equivariant graph-based spherical cnn. *ICLR 2019 Workshop on Representation Learning on Graphs and Manifolds*, 2019.

[14] Octavian-Eugen Ganea, Gary Bécigneul, and Thomas Hofmann. Hyperbolic neural networks. In *Advances in neural information processing systems*, pages 5350–5360, 2018.

[15] Qi Liu, Maximilian Nickel, and Douwe Kiela. Hyperbolic graph neural networks. In Hanna M. Wallach, Hugo Larochelle, Alina Beygelzimer, Florence d'Alché-Buc, Emily B. Fox, and Roman Garnett, editors, *Advances in Neural Information Processing Systems 32: Annual Conference on Neural Information Processing Systems 2019, NeurIPS 2019, December 8-14, 2019, Vancouver, BC, Canada*, pages 8228–8239, 2019.

[16] Shichao Zhu, Shirui Pan, Chuan Zhou, Jia Wu, Yanan Cao, and Bin Wang. Graph geometry interaction learning. In *Advances in Neural Information Processing Systems*, 2020.

[17] Yiding Zhang, Xiao Wang, Chuan Shi, Nian Liu, and Guojie Song. Lorentzian graph convolutional networks. In *International World Wide Web Conference Committee*, 2021.

[18] Jindou Dai, Yuwei Wu, Zhi Gao, and Yunde Jia. A hyperbolic-to-hyperbolic graph convolutional network. In *Proceedings of the IEEE/CVF Conference on Computer Vision and Pattern Recognition*, pages 154–163, 2021.

[19] Albert Gu, Frederic Sala, Beliz Gunel, and Christopher Ré. Learning mixed-curvature representations in product spaces. In *7th International Conference on Learning Representations, ICLR 2019, New Orleans, LA, USA, May 6-9, 2019*. OpenReview.net, 2019.

[20] Ondrej Skopek, Octavian-Eugen Ganea, and Gary Bécigneul. Mixed-curvature variational autoencoders. In *8th International Conference on Learning Representations, ICLR 2020, Addis Ababa, Ethiopia, April 26-30, 2020*. OpenReview.net, 2020.

[21] Julian Laub and Klaus-Robert Müller. Feature discovery in non-metric pairwise data. *The Journal of Machine Learning Research*, 5:801–818, 2004.

[22] James R Clough and Tim S Evans. Embedding graphs in lorentzian spacetime. *PloS one*, 12(11):e0187301, 2017.

[23] Marc T. Law and Jos Stam. Ultrahyperbolic representation learning. In Hugo Larochelle, Marc'Aurelio Ranzato, Raia Hadsell, Maria-Florina Balcan, and Hsuan-Tien Lin, editors, *Advances in Neural Information Processing Systems 33: Annual Conference on Neural Information Processing Systems 2020, NeurIPS 2020, December 6-12, 2020, virtual*, 2020.

[24] Aaron Sim, Maciej Wiatrak, Angus Brayne, Páidí Creed, and Saee Paliwal. Directed graph embeddings in pseudo-riemannian manifolds. *Thirty-eighth International Conference on Machine Learning*, 2021.

[25] Bo Xiong, Shichao Zhu, Mojtaba Nayyeri, Chengjin Xu, Shirui Pan, Chuan Zhou, and Steffen Staab. Ultrahyperbolic knowledge graph embeddings. *Advances in Neural Information Processing Systems*, 2022.

[26] Barrett O'neill. Semi-riemannian geometry with applications to relativity. *Academic pres*, 103, 1983.

[27] Thomas James Willmore. *An introduction to differential geometry*. Courier Corporation, 2013.

[28] Daniel Spiegel. The hopf-rinow theorem. *Notes available online*, 2016.

[29] Fabio Giannoni, Paolo Piccione, and Rosella Sampalmieri. On the geodesical connectedness for a class of semi-riemannian manifolds. *Journal of mathematical analysis and applications*, 252(1):444–476, 2000.

[30] Tingran Gao, Lek-Heng Lim, and Ke Ye. Semi-riemannian manifold optimization. *CoRR*, 2018.

[31] Ines Chami, Zhitao Ying, Christopher Ré, and Jure Leskovec. Hyperbolic graph convolutional neural networks. In Hanna M. Wallach, Hugo Larochelle, Alina Beygelzimer, Florence d'Alché-Buc, Emily B. Fox, and Roman Garnett, editors, *Advances in Neural Information Processing Systems 32: Annual Conference on Neural Information Processing Systems 2019, NeurIPS 2019, December 8-14, 2019, Vancouver, BC, Canada*, pages 4869–4880, 2019.

[32] Gregor Bachmann, Gary Bécigneul, and Octavian Ganea. Constant curvature graph convolutional networks. In *Proceedings of the 37th International Conference on Machine Learning, ICML 2020, 13-18 July 2020, Virtual Event*, volume 119 of *Proceedings of Machine Learning Research*, pages 486–496. PMLR, 2020.

[33] David Gleich, Leonid Zhukov, and Pavel Berkhin. Fast parallel pagerank: A linear system approach. *Yahoo! Research Technical Report YRL-2004-038, available via http://research. yahoo. com/publication/YRL-2004-038. pdf*, 13:22, 2004.

[34] Duncan J Watts and Steven H Strogatz. Collective dynamics of 'small-world'networks. *nature*, 393(6684):440–442, 1998.

[35] Ara Cho, Junha Shin, Sohyun Hwang, Chanyoung Kim, Hongseok Shim, Hyojin Kim, Hanhae Kim, and Insuk Lee. Wormnet v3: a network-assisted hypothesis-generating server for caenorhabditis elegans. *Nucleic acids research*, 42(W1):W76–W82, 2014.

[36] Julian J. McAuley and Jure Leskovec. Learning to discover social circles in ego networks. In Peter L. Bartlett, Fernando C. N. Pereira, Christopher J. C. Burges, Léon Bottou, and Kilian Q. Weinberger, editors, *Advances in Neural Information Processing Systems 25: 26th Annual Conference on Neural Information Processing Systems 2012. Proceedings of a meeting held December 3-6, 2012, Lake Tahoe, Nevada, United States*, pages 548–556, 2012.

[37] William L. Hamilton, Zhitao Ying, and Jure Leskovec. Inductive representation learning on large graphs. In Isabelle Guyon, Ulrike von Luxburg, Samy Bengio, Hanna M. Wallach, Rob Fergus, S. V. N. Vishwanathan, and Roman Garnett, editors, *Advances in Neural Information Processing Systems 30: Annual Conference on Neural Information Processing Systems 2017, December 4-9, 2017, Long Beach, CA, USA*, pages 1024–1034, 2017.

[38] Zhilin Yang, William W. Cohen, and Ruslan Salakhutdinov. Revisiting semi-supervised learning with graph embeddings. In Maria-Florina Balcan and Kilian Q. Weinberger, editors, *Proceedings of the 33nd International Conference on Machine Learning, ICML 2016, New York City, NY, USA, June 19-24, 2016*, volume 48 of *JMLR Workshop and Conference Proceedings*, pages 40–48. JMLR.org, 2016.

[39] Maximilian Nickel and Douwe Kiela. Poincaré embeddings for learning hierarchical representations. In Isabelle Guyon, Ulrike von Luxburg, Samy Bengio, Hanna M. Wallach, Rob Fergus, S. V. N. Vishwanathan, and Roman Garnett, editors, *Advances in Neural Information Processing Systems 30: Annual Conference on Neural Information Processing Systems 2017, December 4-9, 2017, Long Beach, CA, USA*, pages 6338–6347, 2017.

[40] Bhuwan Dhingra, Christopher Shallue, Mohammad Norouzi, Andrew Dai, and George Dahl. Embedding text in hyperbolic spaces. In *Proceedings of the Twelfth Workshop on Graph-Based Methods for Natural Language Processing (TextGraphs-12)*, pages 59–69, New Orleans, Louisiana, USA, 2018. Association for Computational Linguistics.

[41] Ivana Balazevic, Carl Allen, and Timothy M. Hospedales. Multi-relational poincaré graph embeddings. In Hanna M. Wallach, Hugo Larochelle, Alina Beygelzimer, Florence d'Alché-Buc, Emily B. Fox, and Roman Garnett, editors, *Advances in Neural Information Processing Systems 32: Annual Conference on Neural Information Processing Systems 2019, NeurIPS 2019, December 8-14, 2019, Vancouver, BC, Canada*, pages 4465–4475, 2019.

[42] Nurendra Choudhary, Nikhil Rao, Sumeet Katariya, Karthik Subbian, and Chandan K. Reddy. Self-supervised hyperboloid representations from logical queries over knowledge graphs. In *WWW*, pages 1373–1384. ACM / IW3C2, 2021.

[43] Tim R. Davidson, Luca Falorsi, Nicola De Cao, Thomas Kipf, and Jakub M. Tomczak. Hyperspherical variational auto-encoders. In Amir Globerson and Ricardo Silva, editors, *Proceedings of the Thirty-Fourth Conference on Uncertainty in Artificial Intelligence, UAI 2018, Monterey, California, USA, August 6-10, 2018*, pages 856–865. AUAI Press, 2018.

[44] Jiacheng Xu and Greg Durrett. Spherical latent spaces for stable variational autoencoders. In *Proceedings of the 2018 Conference on Empirical Methods in Natural Language Processing*, pages 4503–4513, Brussels, Belgium, 2018. Association for Computational Linguistics.

[45] Zhen Han, Peng Chen, Yunpu Ma, and Volker Tresp. DyERNIE: Dynamic Evolution of Riemannian Manifold Embeddings for Temporal Knowledge Graph Completion. In *Proceedings of the 2020 Conference on Empirical Methods in Natural Language Processing (EMNLP)*, pages 7301–7316, Online, 2020. Association for Computational Linguistics.

[46] Marc Law. Ultrahyperbolic neural networks. *Advances in Neural Information Processing Systems*, 34, 2021.

[47] H Anciaux. Minimal submanifolds in pseudo-riemannian geometry. *World Scientific*, 2011.

[48] Keyulu Xu, Chengtao Li, Yonglong Tian, Tomohiro Sonobe, Ken-ichi Kawarabayashi, and Stefanie Jegelka. Representation learning on graphs with jumping knowledge networks. In Jennifer G. Dy and Andreas Krause, editors, *Proceedings of the 35th International Conference on Machine Learning, ICML 2018, Stockholmsmässan, Stockholm, Sweden, July 10-15, 2018*, volume 80 of *Proceedings of Machine Learning Research*, pages 5449–5458. PMLR, 2018.

[49] Ming Chen, Zhewei Wei, Zengfeng Huang, Bolin Ding, and Yaliang Li. Simple and deep graph convolutional networks. In *Proceedings of the 37th International Conference on Machine Learning, ICML 2020, 13-18 July 2020, Virtual Event*, volume 119 of *Proceedings of Machine Learning Research*, pages 1725–1735. PMLR, 2020.

[50] Yulong Pei, Tianjin Huang, Werner van Ipenburg, and Mykola Pechenizkiy. Resgcn: Attention-based deep residual modeling for anomaly detection on attributed networks. *CoRR*, 2020.

# Appendices

## Broader Impact

Going beyond Riemannian manifolds, we extend GCNs to the pseudo-Riemannian manifolds, which is a smooth manifold furnished with indefinite metric. Our contribution is both theoretical and practical. We introduce necessary geodesic tools in geodesically disconnected pseudo-Riemannian manifolds to help machine learning researchers to define vector operations like matrix multiplication and vector addition. These operations are application agnostic and could be applied in the context of machine learning algorithms. $\mathcal{Q}$-GCN is a flexible framework and is especially powerful on modeling real-world graphs such as social networks and molecular networks which usually exhibit heterogeneous topological structures. We foresee our method can be applied to more practical settings such as recommender systems and drug discovery, and also stimulate more applications of pseudo-Riemannian geometry in machine learning and related communities. However, we emphasize that current models might suffer from the same problems as other deep models such as limited interpretability, and thus, are not capable of replacing human expertise. We advocate researchers to focus more on the interpretability of non-Euclidean graph embeddings.

## A    Notation

In this paper, we denote the points on manifolds by boldface Roman characters. The tangent vectors on tangent spaces are denoted by boldface Greek fonts. The notations are summarized in Table 5.

Table 5: Commonly used notations.

| Notations | Descriptions |
|---|---|
| $\mathcal{Q}_\beta^{s,t}$ | The pseudo-hyperboloid with $s$ space dimensions, $t$ time dimensions, and curvature parameter $\beta$ |
| $\mathbf{x}, \mathbf{y}, \mathbf{z}$ | The points in manifolds |
| $\boldsymbol{\xi}, \boldsymbol{\zeta}$ | The tangent vectors in tangent space |
| $\mathcal{T}_x\mathcal{M}$ | The tangent space at point $\mathbf{x} \in \mathcal{M}$ |
| $\mathbb{R}$ | The Euclidean space |
| $\mathbb{S}$ | The spherical space |
| $\mathbb{H}$ | The hyperbolic space |
| $\mathcal{U}_\mathbf{x}$ | The normal neighborhood of point $\mathbf{x}$ |
| $\gamma_{\mathbf{x}\to\boldsymbol{\xi}}(\tau)$ | The geodesic of mapping a real value $\tau$ to a point on $\mathcal{M}$ with tangent direction $\boldsymbol{\xi} \in \mathcal{T}_\mathbf{x}\mathcal{M}$ |
| $\exp, \log$ | The exponential and logarithmic maps |
| $\widehat{\exp}, \widehat{\log}$ | The diffeomorphic exponential and logarithmic maps |
| $P_{\mathbf{x}\to\mathbf{y}}^\beta(\boldsymbol{\xi})$ | The parallel transport of tangent vector on $\mathcal{T}_\mathbf{x}\mathcal{M}$ with direction $\boldsymbol{\xi} \in \mathcal{T}_\mathbf{x}\mathcal{M}$ to another tangent space $\mathcal{T}_\mathbf{y}\mathcal{M}$ |
| $\psi$ | The diffeomorphic function |
| $\otimes^\beta$ | Pseudo-hyperboloid multiplication |
| $\oplus^\beta$ | Pseudo-hyperboloid addition |

## B    Related Works

**Riemannian embedding.** Non-Euclidean Riemannian spaces have recently gained extensive attention in learning representation for non-euclidean data. [39] was the first work to learn hierarchical embeddings in hyperbolic space for link prediction. Following this work, [40] applied hyperbolic embedding in word embedding. [41] proposed a translation model in hyperbolic space for multi-relational graph embedding, and [42] proposed a hyperbolic embedding for answering complex logical queries. On the other hand, spherical space offers benefits for embedding spherical or cyclical data [13, 43, 44]. For mixed curvature space, product manifolds [19, 20] on Euclidean, hyperbolic

and spherical space has been proposed to embed graph and knowledge graphs [45] with mixed structures. HNN [14] extended neural networks into the hyperbolic space and defined some fundamental neural operations.

**Riemannian GCN.** Going beyond GCNs in Euclidean space [1, 2], HGNN [15] and HGCN [31] first extended GCNs into hyperbolic space, achieving state-of-the-art performance on learning graph embedding for scale-free networks. The main solution is to move the graph convolutional operations (e.g. *feature transformation*, *aggregation*) into the *tangent space* of manifolds and perform Euclidean operations on the space. To model graphs of mixed topologies, $\kappa$-GCN [32] unifies curvatures in a $\kappa$-stereographic model and extends GCNs into the products of Riemannian projection manifolds. GIL [16] proposed graph geometric interaction learning that models interaction between hyperbolic and Euclidean space. Different from these works, $\mathcal{Q}$-GCN learns graph embeddings in a single pseudo-Riemannian space with indefinite metrics while capturing mixed graph structures.

**Pseudo-Riemannian machine learning.** Few works [5, 30, 23, 24, 22] have explored the application of pseudo-Riemannian geometry in machine learning. [5] first applied pseudo-Riemannian geometry (or *pseudo-Euclidean space*) to embed non-metric data that preserves local information. [22] exploited Lorentzian spacetime on embedding directed acyclic graphs, [30] developed a manifold learning framework on the pseudo-Riemannian manifold and its submanifolds. More recently, [23] proposed learning graph embeddings on pseudo-hyperboloid and provided some geodesic tools. [24] further extended it into directed graph embedding with novel tools. [46] first studied the pseudo-Riemannian geometry in the setting of deep learning. However, their embedding is learned in a quotient manifold. Different from [46], our embedding is directly learned from the pseudo-hyperboloid.

## C   Review of Pseudo-Riemannian Geometry

### C.1   Pseudo-Riemannian manifold

The pseudo-Riemannian manifold $\mathcal{M}$ is equipped with a pseudo-Riemannian metric $g_{\mathbf{x}} : \mathcal{T}_{\mathbf{x}}\mathcal{M} \times \mathcal{T}_{\mathbf{x}}\mathcal{M}$ at point $\mathbf{x}$. The metric $g_{\mathbf{x}}$ is a nondegenerate symmetric bilinear form, which means that if for a given $\boldsymbol{\xi} \in \mathcal{T}_{\mathbf{x}}\mathcal{M}$, for any $\boldsymbol{\zeta} \in \mathcal{T}_{\mathbf{x}}\mathcal{M}$ we have $g_{\mathbf{x}}(\boldsymbol{\xi}, \boldsymbol{\zeta}) = 0$, then $\boldsymbol{\xi} = \mathbf{0}$. The $\mathcal{M}$ manifold has the constant sectional curvature of $1/\beta$ and constant mean curvature $\kappa = |\beta|^{-1/2}$. We recommend the reader to refer [26, 47] for details.

### C.2   Geodesic tools of pseudo-hyperboloid

Although pseudo-hyperboloid is a *geodescially disconnected* manifold, previous works [23, 30] have defined some standard geodesic tools that do not consider the broken cases which we recall below.

**Geodesic.** The geodesics of pseudo-hyperboloid are a combination of the hyperbolic, flat and spherical cases, depending on the sign of $\langle \boldsymbol{\xi}, \boldsymbol{\xi} \rangle_t$. Formally, the geodesic $\gamma_{\mathbf{x} \to \boldsymbol{\xi}}(\tau)$ of $\mathcal{Q}_{\beta}^{s,t}$ with $\beta < 0$ is defined as Eq. (8).

$$
\gamma_{\mathbf{x} \to \boldsymbol{\xi}}(\tau) = \begin{cases} \cosh\left(\frac{\tau\sqrt{|\langle \boldsymbol{\xi}, \boldsymbol{\xi} \rangle_t|}}{\sqrt{|\beta|}}\right)\mathbf{x} + \frac{\sqrt{|\beta|}}{\sqrt{\langle \boldsymbol{\xi}, \boldsymbol{\xi} \rangle_t}}\sinh\left(\frac{\tau\sqrt{|\langle \boldsymbol{\xi}, \boldsymbol{\xi} \rangle_t|}}{\sqrt{|\beta|}}\right), & \text{if } \langle \boldsymbol{\xi}, \boldsymbol{\xi} \rangle_t > 0 \\ \mathbf{x} + \tau\boldsymbol{\xi}, & \text{if } \langle \boldsymbol{\xi}, \boldsymbol{\xi} \rangle_t = 0 \\ \cos\left(\frac{\tau\sqrt{|\langle \boldsymbol{\xi}, \boldsymbol{\xi} \rangle_t|}}{\sqrt{|\beta|}}\right)\mathbf{x} + \frac{\sqrt{|\beta|}}{\sqrt{\langle \boldsymbol{\xi}, \boldsymbol{\xi} \rangle_t}}\sin\left(\frac{\tau\sqrt{|\langle \boldsymbol{\xi}, \boldsymbol{\xi} \rangle_t|}}{\sqrt{|\beta|}}\right) & \text{if } \langle \boldsymbol{\xi}, \boldsymbol{\xi} \rangle_t < 0 \end{cases} \tag{8}
$$

**Exponential and logarithmic maps.** The exponential and logarithmic maps in the pseudo-hyperboloid manifold are defined as $\exp_{\mathbf{x}} : \mathcal{T}_{\mathbf{x}}\mathcal{Q}_{\beta}^{s,t} \to \mathcal{Q}_{\beta}^{s,t}$ and $\log_{\mathbf{x}} : \mathcal{Q}_{\beta}^{s,t} \to \mathcal{T}_{\mathbf{x}}\mathcal{Q}_{\beta}^{s,t}$, respectively. We have the following closed form expressions of the exponential and the logarithmic maps [23], which allow us to perform operations on points on the pseudo-hyperboloid or pseudo-sphere manifolds by mapping them to *tangent* spaces and vice-versa, formally given by

$$
\exp_{\mathbf{x}}(\boldsymbol{\xi}) = \begin{cases} \cosh\left(\frac{\sqrt{\langle \boldsymbol{\xi}, \boldsymbol{\xi} \rangle}}{\sqrt{|\beta|}}\right)\mathbf{x} + \frac{\sqrt{|\beta|}}{\sqrt{\langle \boldsymbol{\xi}, \boldsymbol{\xi} \rangle}}\sinh\left(\frac{t\sqrt{\langle \boldsymbol{\xi}, \boldsymbol{\xi} \rangle}}{\sqrt{|\beta|}}\right)\boldsymbol{\xi}, & \text{if}\langle \boldsymbol{\xi}, \boldsymbol{\xi} \rangle > 0 \\ \mathbf{x} + \boldsymbol{\xi}, & \text{if } \langle \boldsymbol{\xi}, \boldsymbol{\xi} \rangle = 0 \\ \cos\left(\frac{\sqrt{\langle \boldsymbol{\xi}, \boldsymbol{\xi} \rangle}}{\sqrt{|\beta|}}\right)\mathbf{x} + \frac{\sqrt{|\beta|}}{\sqrt{\langle \boldsymbol{\xi}, \boldsymbol{\xi} \rangle}}\sin\left(\frac{\sqrt{\langle \boldsymbol{\xi}, \boldsymbol{\xi} \rangle}}{\sqrt{|\beta|}}\right)\boldsymbol{\xi}, & \text{if } \langle \boldsymbol{\xi}, \boldsymbol{\xi} \rangle < 0 \end{cases} \tag{9}
$$

$$\log_{\mathbf{x}}(\mathbf{y}) = \begin{cases} \dfrac{\cosh^{-1}\left(\frac{\langle x,y\rangle_t}{\beta}\right)}{\sqrt{\left(\frac{\langle x,y\rangle_t}{\beta}\right)^2-1}}\left(\mathbf{y}-\frac{\langle \mathbf{x},\mathbf{y}\rangle_t}{\beta}\mathbf{x}\right), & \text{if } \frac{\langle \mathbf{x},\mathbf{y}\rangle_t}{|\beta|} < -1 \\[2mm] \mathbf{y}-\mathbf{x}, & \text{if } \frac{\langle \mathbf{x},\mathbf{y}\rangle_t}{|\beta|} = -1 \\[2mm] \dfrac{\cos^{-1}\left(\frac{\langle \mathbf{x},\mathbf{y}\rangle_t}{\beta}\right)}{\sqrt{1-\left(\frac{\langle \mathbf{x},\mathbf{y}\rangle_t}{\beta}\right)^2}}\left(\mathbf{y}-\frac{\langle \mathbf{x},\mathbf{y}\rangle_t}{\beta}\mathbf{x}\right), & \text{if } \frac{\langle \mathbf{x},\mathbf{y}\rangle_t}{|\beta|} \in (-1,1) \end{cases} \tag{10}$$

It is worth mentioning that not all points on the pseudo-hyperboloid manifold are connected by a geodesic. For these broken points, there does not exist a tangent vector $\boldsymbol{\xi}$ such that $\mathbf{y} = \exp_{\mathbf{x}}(\boldsymbol{\xi})$. Namely, the logarithmic map is not defined if $\langle \mathbf{x},\mathbf{y}\rangle \geq |\beta|$.

**Distance.** By the means of the geodesic, the distance between $\mathbf{x}$ and $\mathbf{y}$ in pseudo-Riemannian manifolds $\mathcal{Q}_\beta^{s,t}$ is defined as the arc length of geodesic $\gamma(\tau)$, given by Eq. (11).

$$d(\mathbf{x},\mathbf{y}) = \sqrt{\left| \|\log_{\mathbf{x}}(\mathbf{y})\|_t^2 \right|}. \tag{11}$$

**Parallel transport.** Given the geodesic $\gamma(\tau)$ on $\mathcal{Q}_\beta^{s,t}$ passing through $\mathbf{x} \in \mathcal{Q}_\beta^{s,t}$ with the tangent direction $\boldsymbol{\xi} \in \mathcal{T}_{\mathbf{x}}\mathcal{Q}_\beta^{s,t}$, the parallel transport of $\boldsymbol{\zeta} \in \mathcal{T}_{\mathbf{x}}\mathcal{Q}_\beta^{s,t}$ is defined as Eq. (12).

$$P_{\mathbf{x}\to\mathbf{y}}^\beta(\boldsymbol{\xi}) = \begin{cases} \frac{\langle \boldsymbol{\zeta},\boldsymbol{\xi}\rangle}{\|\boldsymbol{\xi}\|}\left[\mathbf{x}\sinh(\tau\|\boldsymbol{\xi}\|)+\frac{\boldsymbol{\xi}}{\|\boldsymbol{\xi}\|}\cosh(\tau\|\boldsymbol{\xi}\|)\right]+\left(\boldsymbol{\zeta}-\frac{\langle \boldsymbol{\zeta},\boldsymbol{\xi}\rangle}{\|\boldsymbol{\xi}\|^2}\boldsymbol{\xi}\right), & \text{if } \langle \boldsymbol{\xi},\boldsymbol{\xi}\rangle > 0 \\[2mm] \frac{\langle \boldsymbol{\zeta},\boldsymbol{\xi}\rangle}{\|\boldsymbol{\xi}\|}\left[\mathbf{x}\sin(\tau\|\boldsymbol{\xi}\|)-\frac{\boldsymbol{\xi}}{\|\boldsymbol{\xi}\|}\cos(\tau\|\boldsymbol{\xi}\|)\right]+\left(\boldsymbol{\zeta}+\frac{\langle \boldsymbol{\zeta},\boldsymbol{\xi}\rangle}{\|\boldsymbol{\xi}\|^2}\boldsymbol{\xi}\right), & \text{if } \langle \boldsymbol{\xi},\boldsymbol{\xi}\rangle < 0 \\[2mm] \langle \boldsymbol{\zeta},\boldsymbol{\xi}\rangle\left(\tau\mathbf{x}+\frac{1}{2}\tau^2\boldsymbol{\xi}\right)+\boldsymbol{\zeta}, & otherwise \end{cases} \tag{12}$$

where $\boldsymbol{\xi} = \log_{\mathbf{x}}(\mathbf{y})$.

# D Proof of Theorems

## D.1 Proof of Theorem 1

**Theorem 1** (Theorem 4.1 in [23]). *For any point* $\mathbf{x} \in \mathcal{Q}_\beta^{s,t}$*, there exists a diffeomorphism* $\psi :$ $\mathcal{Q}_\beta^{s,t} \to \mathbb{S}_1^t \times \mathbb{R}^s$ *that maps* $\mathbf{x}$ *into the product manifolds of an unit sphere and the Euclidean space, the mapping and its inverse are given by,*

$$\psi(\mathbf{x}) = \begin{pmatrix} \frac{1}{\|t\|}\mathbf{t} \\ \frac{1}{\sqrt{|\beta|}}\mathbf{s} \end{pmatrix}, \quad \psi^{-1}(\mathbf{z}) = \sqrt{|\beta|}\begin{pmatrix} \sqrt{1+\|\mathbf{v}\|^2}\mathbf{u} \\ \mathbf{v} \end{pmatrix}, \tag{13}$$

*where* $\mathbf{x} = \begin{pmatrix} \mathbf{t} \\ \mathbf{s} \end{pmatrix} \in \mathcal{Q}_\beta^{s,t}$ *with* $\mathbf{t} \in \mathbb{R}_*^{t+1}$ *and* $\mathbf{s} \in \mathbb{R}^s$*.* $\mathbf{z} = \begin{pmatrix} \mathbf{u} \\ \mathbf{v} \end{pmatrix} \in \mathbb{S}_1^t \times \mathbb{R}^s$ *with* $\mathbf{u} \in \mathbb{S}_1^t$ *and* $\mathbf{v} \in \mathbb{R}^s$*.*

Please refer Appendix C.5 in [23] for proof of this theorem.

## D.2 Proof of Theorem 2

**Theorem 2.** *For any point* $\mathbf{x} \in \mathcal{Q}_\beta^{s,t}$*, there exists a diffeomorphism* $\psi : \mathcal{Q}_\beta^{s,t} \to \mathbb{S}_{-\beta}^t \times \mathbb{R}^s$ *that maps* $\mathbf{x}$ *into the product manifolds of a sphere and the Euclidean space, the mapping and its inverse are given by,*

$$\psi(\mathbf{x}) = \begin{pmatrix} \sqrt{|\beta|}\frac{\mathbf{t}}{\|\mathbf{t}\|} \\ \mathbf{s} \end{pmatrix}, \quad \psi^{-1}(\mathbf{z}) = \begin{pmatrix} \frac{\sqrt{|\beta|+\|\mathbf{v}\|^2}}{\sqrt{|\beta|}}\mathbf{u} \\ \mathbf{v} \end{pmatrix}, \tag{14}$$

*where* $\mathbf{x} = \begin{pmatrix} \mathbf{t} \\ \mathbf{s} \end{pmatrix} \in \mathcal{Q}_\beta^{s,t}$ *with* $\mathbf{t} \in \mathbb{R}_*^t$ *and* $\mathbf{s} \in \mathbb{R}^s$*.* $\mathbf{z} = \begin{pmatrix} \mathbf{u} \\ \mathbf{v} \end{pmatrix} \in \mathbb{S}_{-\beta}^t \times \mathbb{R}^s$ *with* $\mathbf{u} \in \mathbb{S}_{-\beta}^t$ *and* $\mathbf{v} \in \mathbb{R}^s$*.*

*Proof.* It is easy to show that the $\psi$ and $\psi^{-1}$ are smooth functions as they only involve with a linear mapping with a constant scaling vector. Hence, we only need to show that $\psi\left(\psi^{-1}(\mathbf{z})\right) = \mathbf{z}$ and $\psi^{-1}(\psi(\mathbf{x})) = \mathbf{x}$. Here, we consider space dimensions and time dimensions separately.

For space dimensions, the mapping of the space dimensions of $\mathbf{x}$ to the space dimensions of $\mathbf{z}$ is an identity function (i.e. $\mathbf{v} = \mathbf{s}, \mathbf{s} = \mathbf{v}$). Thus, we only need to show the invertibility of the mappings taking time dimensions as inputs. For time dimensions, we first show that:

$$\psi^{-1}(\psi(\mathbf{t})) = \frac{\sqrt{|\beta| + \|\mathbf{v}\|^2}}{\sqrt{|\beta|}} \sqrt{|\beta|} \frac{\mathbf{t}}{\|\mathbf{t}\|} = \sqrt{|\beta| + \|\mathbf{v}\|^2} \frac{\mathbf{t}}{\|\mathbf{t}\|}$$
$$= \sqrt{|\beta| + \|\mathbf{s}\|^2} \frac{\mathbf{t}}{\|\mathbf{t}\|} = \|\mathbf{t}\| \frac{\mathbf{t}}{\|\mathbf{t}\|} = \mathbf{t}. \tag{15}$$

Note that the last equality can be inferred by the fact that $\mathbf{x} \in \mathcal{Q}_\beta^{s,t}$ and $\beta < 0$. We then show that:

$$\psi(\psi^{-1}(\mathbf{u})) = \sqrt{|\beta|} \frac{\sqrt{|\beta| + \|\mathbf{v}\|^2}}{\sqrt{|\beta|}} \frac{\mathbf{u}}{\|\frac{\sqrt{|\beta| + \|\mathbf{v}\|^2}}{\sqrt{|\beta|}} \mathbf{u}\|} = \sqrt{|\beta|} \frac{\mathbf{u}}{\|\mathbf{u}\|} = \mathbf{u}. \tag{16}$$

Note that the last equality can be inferred by the fact that $\mathbf{u} \in \mathbb{S}_{-\beta}^t$ and $\beta < 0$. $\qquad\square$

### D.3 Proof of Theorem 3

**Theorem 3.** *For any reference point* $\mathbf{x} = \begin{pmatrix} \mathbf{t} \\ \mathbf{s} \end{pmatrix} \in \mathcal{Q}_\beta^{s,t}$ *with space dimension* $\mathbf{s} = \mathbf{0}$, *the induced tangent space of* $\mathcal{Q}_\beta^{s,t}$ *is equal to the tangent space of its diffeomorphic manifold* $\mathbb{S}_{-\beta}^t \times \mathbb{R}^s$, *namely,* $\mathcal{T}_{\psi(\mathbf{x})}(\mathbb{S}_{-\beta}^t \times \mathbb{R}^s) = \mathcal{T}_\mathbf{x} \mathcal{Q}_\beta^{s,t}$.

*Proof.* For any point $\mathbf{x} = \begin{pmatrix} \mathbf{t} \\ \mathbf{s} \end{pmatrix} \in \mathcal{Q}_\beta^{s,t}$ with $\mathbf{s} = \mathbf{0}$, the corresponding point in the diffeomorphic manifold is $\psi(\mathbf{x}) = \begin{pmatrix} \sqrt{|\beta|} \frac{\mathbf{t}}{\|\mathbf{t}\|} \\ \mathbf{0} \end{pmatrix}$. Based on the definition of tangent space, for any tangent vector $\boldsymbol{\xi} \in \mathcal{T}_\mathbf{x} \mathcal{Q}_\beta^{s,t}$, $\langle \mathbf{x}, \boldsymbol{\xi} \rangle_t = 0$ implies $-\mathbf{t}\boldsymbol{\xi}_t + \mathbf{0}\boldsymbol{\xi}_s = 0$, which means $\mathbf{t}\boldsymbol{\xi}_t = 0$. Thus, $\langle \psi(\mathbf{x}), \boldsymbol{\xi} \rangle_t = 0$. Based on the definition of tangent space, $\boldsymbol{\xi} \in \mathcal{T}_{\psi(\mathbf{x})}(\mathbb{S}_{-\beta}^t \times \mathbb{R}^s)$. $\qquad\square$

### D.4 Proof of Theorem 4

**Theorem 4.** *For any point* $\mathbf{x} \in \mathcal{Q}_\beta^{s,t}$, *the union of the normal neighborhood of* $\mathbf{x}$ *and the normal neighborhood of its antipodal point* $-\mathbf{x}$ *cover the entire manifold. Namely,* $\mathcal{U}_\mathbf{x} \cup \mathcal{U}_{-\mathbf{x}} = \mathcal{Q}_\beta^{s,t}$.

*Proof.* For any point $\mathbf{x} \in \mathcal{Q}_\beta^{s,t}$ and $\mathbf{y} \notin \mathcal{U}_x$. Based on the definition of normal neighborhood, $\langle \mathbf{x}, \mathbf{y} \rangle_t \geq |\beta| \rightarrow \langle -\mathbf{x}, \mathbf{y} \rangle_t \leq |\beta|$. Thus, $\mathbf{y} \in \mathcal{U}_{-x}$, and $\mathcal{U}_\mathbf{x} \cup \mathcal{U}_{-\mathbf{x}} = \mathcal{Q}_\beta^{s,t}$. $\qquad\square$

## E   Supplementary experimental details

In this section, we present the details of our experiments and implementations, as well as some additional analyses.

### E.1   Graph Reconstruction

For graph reconstruction, one straightforward method is to minimize the graph distortion [32, 19] given by

$$\frac{1}{|V|^2} \sum_{u,v} \left( \left( \frac{d(\mathbf{u}, \mathbf{v})}{d_G(u, v)} \right)^2 - 1 \right)^2, \tag{17}$$

where $d(\mathbf{u}, \mathbf{v})$ is the distance function in the embedding space and $d_G(u, v)$ is the graph distance (the length of shortest path) between node $u$ and $v$, $|V|$ is the number of nodes in graph. The objective function is to preserve all pairwise graph distances. Motivated by the fact that most of graphs are partially observable, we minimize an alternative loss function [23, 39] that preserves local graph distance, given by,

$$\mathcal{L}(\Theta) = \sum_{(u,v)\in\mathcal{D}} \log \frac{e^{-d(\mathbf{u},\mathbf{v})}}{\sum_{\mathbf{v}'\in\mathcal{E}(u)} \exp^{-d(\mathbf{u},\mathbf{v}')}}, \quad (18)$$

where $\mathcal{D}$ is the connected relations in the graph, $\mathcal{E}(u) = \{v|(u,v) \notin D \cup u\}$ is the set of negative examples for node $u$, $d(\mathbf{u}, \mathbf{v})$ is the distance function in the embedding space. For evaluation, we apply the mean average precision (mAP) to evaluate the graph reconstruction task. mAP is a local metric that measures the average proportion of the nearest points of a node which are actually its neighbors in the original graph. The mAP is defined as Eq. (19).

$$\mathrm{mAP}(f) = \frac{1}{|V|} \sum_{u\in V} \frac{1}{\deg(u)} \sum_{i=1}^{|\mathcal{N}_u|} \frac{|\mathcal{N}_u \cap R_{u,v_i}|}{|R_{u,v_i}|}, \quad (19)$$

where $f$ is the embedding function, $|V|$ is the number of nodes in graph, $\deg(u)$ is the degree of node $u$, $\mathcal{N}_u$ is the one-hop neighborhoods in the graph, $\mathbb{R}_{u,v}$ denotes whether two nodes $u$ and $v$ are connected.

**Implementation details.** We implement our models by Pytorch and *Geoopt* tool[3]. Our models and baselines are built upon the codes[4]. For baselines of product space and $\kappa$-GCN, we use the code[5]. Our models are trained on NVIDIA A100 with 4 GPU cards. Similar to [31], we use the pre-tranined embeddings on link prediction as the initialization of node classification, to preserve graph structures information. All non-Euclidean methods do not use attention mechanism for a fair comparison. For node classification and link prediction, the optimal hyper-parameters for all methods are obtained by the same grid search strategy. The ranges of grid search are summarized in Table 6.

Table 6: The grid search space for the hyperparameters.

| Hyperparameter | Search space |
| --- | --- |
| Number of layers | 1,2,3 |
| Weight decay | 0, 1e-3, 5e-4,1e-4 |
| Dropout rate | 0,0.1,0.2,0.3,0.4,0.5,0.6,0.7 |
| Activation | relu, tanh, sigmoid, elu |

**Numerical instability.** In practice, we find that the numerical computation in pseudo-hyperboloid is not stable due to the limited machine precision and rounding. To ensure the learned embeddings and tangent vectors to remain on the manifold and tangent spaces, we conduct projection operations via Eq. (20) and Eq. (21) after each vector operations.

$$\varphi(x) = \psi^{-1} \circ \psi, \quad (20)$$

where $\psi$ can be instantiated by Theorem 2. Note that $\psi(\cdot)$ is an identity function when $\mathbf{x}$ is already localted in $\mathcal{Q}_\beta^{s,t}$. For input $\mathbf{x} \notin \mathcal{Q}_\beta^{s,t}$, applying $\psi(\cdot)$ can project the $\mathbf{x}$ back to $\mathcal{Q}_\beta^{s,t}$, from which $\psi(\cdot)$ is no longer an identity.

$$\Pi_{\mathbf{x}}(\mathbf{z}) = \mathbf{z} - \frac{\langle \mathbf{z}, \mathbf{x}\rangle_t}{\langle \mathbf{x}, \mathbf{x}\rangle_t}\mathbf{x}, \quad (21)$$

where $\mathbf{z}$ is the tangent vector to be projected.

**Trainable curvature.** Similar to the trainable curvature in the hyperbolic space [31], we give an analogue of Theorem 4.1 in [31] as following corollary.

**Corollary 1.** *For any two points* $\mathbf{x}, \mathbf{y} \in \mathcal{Q}_\beta^{s,t}$*, there exists a mapping* $\phi : \mathcal{Q}_\beta^{s,t} \to \mathcal{Q}_{\beta'}^{s,t}$ *that maps* $\mathbf{x}, \mathbf{y}$ *into* $\mathbf{x}', \mathbf{y}' \in \mathcal{Q}_{\beta'}^{s,t}$*, such that the pseudo-Riemannian inner product is scaled by a constant factor* $\frac{\beta'}{\beta}$*. Namely* $\langle \mathbf{x}, \mathbf{y}\rangle_t = \frac{\beta'}{\beta}\langle \mathbf{x}', \mathbf{y}'\rangle_t$*. The mapping is given by* $\phi(\mathbf{x}) = \sqrt{\frac{\beta'}{\beta}}\mathbf{x}$*.*

---

[3]https://github.com/geoopt/geoopt
[4]https://github.com/HazyResearch/hgcn, https://github.com/CheriseZhu/GIL
[5]https://github.com/fal025/producthgcn

Corollary 1 shows that assuming infinite machine precision, pseudo-hyperboloids of varying curvatures should have the same expressive power. However, due to the limited machine precision [31], we set the curvature $1/\beta$ as a trainable parameter to capture the best scale of the embeddings.

**Skip connection.** In preliminary experiments of graph reconstruction, we found that the performance of GCN, HGCN, $\kappa$-GCN and $\mathcal{Q}$-GCN could not compete with the method in [19] that directly optimizes the distance function. We hypothesized that this was probably caused by over-smoothing of graph convolution kernel. Therefore, we decided to apply skip-connection strategy [48, 49, 50] to avoid oversmoothing. Specifically, we take the mean of the hidden output of each layer to the decoder. In the paper, we report the graph reconstruction results of GCN, HGCN, $\kappa$-GCN and $\mathcal{Q}$-GCN applied with skip-connection.

**Dataset analysis.** Table 7 and Table 8 summarize the statistics of the datasets we used for our experiments. For each dataset, we report the number of nodes, the number of edges, the number of classes and the feature dimensions. Besides, we measure the graph sectional curvature to identify the dominating geometry of each dataset. Fig. 4 shows the histograms of sectional curvature and the mean sectional curvature for all datasets. It can be seen that all datasets have both positive and negative sectional curvatures, showcasing that all graphs contain mixed geometric structures. However, the datasets possess a preference for the negative half sectional curvature except the case of Facebook that has dominating positive sectional curvature, showcasing that most of real-world graphs exhibit more hierarchical structures than cyclic structures.

To further analyze the degree of hierarchy of each graph, we apply $\delta$-hyperbolicity to identify the tree-likeness. Table 9 shows the $\delta$-hyperbolicity of different datasets. It shows that although most of the datasets have negative mean sectional curvature, their degrees of hierarchy vary significantly. For example, Airport and Pubmed are more hierarchical than CiteSeer and Cora.

Table 7: A summary of characteristics of the datasets for graph reconstruction.

| Dataset | Power | Bio-Worm | Web-Edu | Facebook |
|---------|-------|----------|---------|----------|
| #Nodes  | 4941  | 2274     | 3031    | 4039     |
| #Edges  | 6594  | 78328    | 6474    | 88234    |

Table 8: A summary of characteristics of the datasets for node classification and link prediction.

| Dataset   | Airport | Pubmed | CiteSeer | Cora |
|-----------|---------|--------|----------|------|
| #Nodes    | 3188    | 19717  | 3327     | 2708 |
| #Edges    | 18631   | 44338  | 4732     | 5429 |
| #Classes  | 4       | 3      | 6        | 7    |
| #Features | 4       | 500    | 3703     | 1433 |

Table 9: The $\delta$-hyperbolicity distribution of all used datasets.

| Datasets | 0 | 0.5 | 1.0 | 1.5 | 2.0 | 2.5 |
|----------|--------|--------|--------|--------|--------|--------|
| Power    | 0.4025 | 0.1722 | 0.1436 | 0.0773 | 0.0639 | 0.0439 |
| Bio-Worm | 0.5635 | 0.3949 | 0.0410 | 0      | 0      | 0      |
| Web-Edu  | 0.9532 | 0.0468 | 0      | 0      | 0      | 0      |
| Facebook | 0.8209 | 0.1569 | 0.0221 | 0      | 0      | 0      |
| Airport  | 0.6376 | 0.3563 | 0.0061 | 0      | 0      | 0      |
| Pubmed   | 0.4239 | 0.4549 | 0.1094 | 0.0112 | 0.0006 | 0      |
| CiteSeer | 0.3659 | 0.3538 | 0.1699 | 0.0678 | 0.0288 | 0      |
| Cora     | 0.4474 | 0.4073 | 0.1248 | 0.0189 | 0.0016 | 0.0102 |

Algorithm 1 describes the training process of the proposed method.
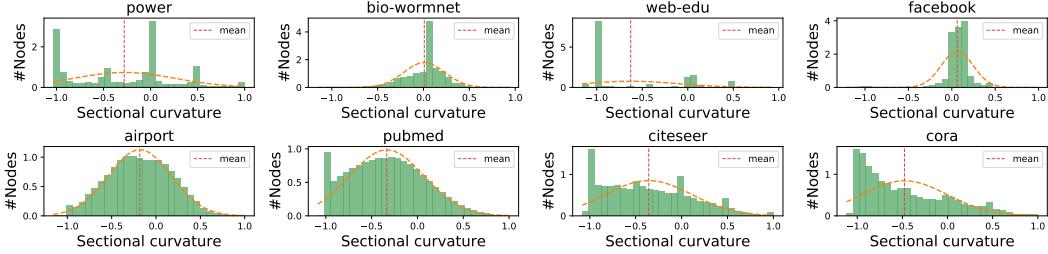
Figure 4: The histograms of sectional curvature for all used datasets.

---

**Algorithm 1** The pseudo-code of $\mathcal{Q}$-GCN

---

**Input:**

    The input graph $\mathcal{G} = (\mathcal{V}, \mathcal{E})$, the input node features $\mathbf{x}$, the time dimension $t$, the space dimension $s$, the initial curvature $\beta$, the number of epoches $E$, the number of layers $L$, the initial learning rate, the activation function $\sigma$, the layer-wise trainable weight $\mathbf{W}$ and bias term $\mathbf{b}$.

**Output:**

    The trained model, i.e., the parameters $\mathbf{W}$, $\mathbf{b}$ and $\beta$. The resulting embeddings $\mathbf{h}$ of nodes.

1: **Feature initialization:** map the input Euclidean features $\mathbf{x}$ into Pseudo-Riemannian space by the double projection $\mathbf{h}^0 = (\psi^{-1} \circ \psi)(\mathbf{x})$ where $\psi$ and $\psi^{-1}$ are given by     ▷*Eq. (5)*.

2: **for** $e \in [0, E)$ **do**

3:     **for** $l \in [0, L)$ **do**

4:         **for** $i \in \mathcal{V}$ **do**

5:             $\mathbf{h}_i^\ell = W^\ell \otimes^\beta \mathbf{h}_i^\ell := \widehat{\exp}_{\mathbf{o}}^\beta \left( W^\ell \widehat{\log}_{\mathbf{o}}^\beta \left( \mathbf{h}_i^\ell \right) \right)$ (**Feature transformation**)

6:             $\mathbf{h}_i^\ell = \widetilde{\mathbf{h}}_i^{\ell} \oplus^\beta \mathbf{b}^\ell := \begin{cases} \exp_{\widetilde{\mathbf{h}}_i^\ell}^\beta \left( P_{\mathbf{o} \to \widetilde{\mathbf{h}}_i^\ell}^\beta \left( \mathbf{b}^\ell \right) \right), & \text{if } \left\langle \mathbf{o}, \widetilde{\mathbf{h}}_i^{\ell} \right\rangle_t < |\beta| \\ -\exp_{-\widetilde{\mathbf{h}}_i^\ell}^\beta \left( P_{\mathbf{o} \to -\widetilde{\mathbf{h}}_i^\ell}^\beta \left( \mathbf{b}^\ell \right) \right), & \text{if } \left\langle \mathbf{o}, \widetilde{\mathbf{h}}_i^{\ell} \right\rangle_t \geq |\beta| \end{cases}$ (**Bias**

        **translation**)

7:             $\mathbf{h}_i^{\ell+1} = \widehat{\exp}_{\mathbf{o}}^{\beta_{\ell+1}} \left( \sigma \left( \sum_{j \in \mathcal{N}(i) \cup \{i\}} \widehat{\log}_{\mathbf{o}}^{\beta_\ell} \left( \mathbf{h}_j^\ell \right) \right) \right)$ (**Neighborhood aggregation**)

8:         **end for**

9:         //Computing the task-dependent loss $\mathcal{L}$.

10:         //Updating the model parameters $\mathbf{W}$, $\mathbf{b}$, and $\beta$ using Adam optimizer.

11:         **if** convergence **then**

12:             break loop.

13:         **end if**

14:     **end for**

15: **end for**

16: //Task-dependent inference.

17: **return** $\mathbf{W}$, $\mathbf{b}$, $\beta$ and $\mathbf{h}$.

---